# Application of the Frozen Gaussian Approximation with Stochastic Surface-Hopping to Nonadiabatic Photochemistry

**Samuel Whitby**

St John’s College

University of Oxford

A Thesis Submitted for the

Honour School of Chemistry:

Chemistry Part II, 2017

Physical and Theoretical Chemistry Laboratory

Oxford, June 2017

# Summary

In this thesis, we investigate a new semiclassical method for simulating nonadiabatic dynamics in photochemical processes. Nonadiabaticity is observed in systems where the Born-Oppenheimer approximation breaks down, allowing non-radiative changes to take place between the electronic states as a result of nuclear motion.[1] This method extends the Frozen Gaussian Approximation[2], a semiclassical solution to the Time Dependent Schrödinger equation for a single electronic state, to nonadiabatic systems that have coupled electronic states. To account for the coupling, a stochastic surface hopping algorithm, in which classical trajectories can hop between the adiabatic surfaces, is employed.[3] As in the Frozen Gaussian Approximation, this method, which we call the 'Frozen Gaussian Approximation with Surface Hopping' (FGA-SH) captures important quantum mechanical coherence via the inclusion of a complex prefactor. The motivation for treating the dynamics semiclassically is to avoid the computational cost associated with quantum mechanical techniques, which require basis sets whose size scales exponentially with the number of nuclear degrees of freedom.

To test the efficacy of this theory, we simulated the gas phase absorption spectrum of pyrazine, a benchmark for nonadiabatic methods. On photoexcitation to its first and second excited singlet states, the dynamics have substantial nonadiabatic character due to the presence of a conical intersection.[4] This results in a complex absorption spectrum that exhibits extensive vibronic coupling.

We first considered a small scale model for pyrazine which retains only a few nuclear degrees of freedom. This model accurately accounts for most of the nonadiabatic behaviour, but is sufficiently small that absorption spectra can generated quan-

tum mechanically for comparison. Initially, FGA-SH simulations on this reduced dimensionality model were found to be numerically intractable for even short-term dynamics, due to the need to evaluate an oscillatory integrand. To remedy this, a 'prefactor damping' algorithm was developed, which reduces the variance of the integrand by suppressing trajectories that contribute the largest magnitudes. This enabled semiclassical simulations to be performed, which gave very good agreement with the quantum calculations.

The theory was then tested on a fully parametrised model of pyrazine.[**5**] This model is too large for straightforward quantum mechanical treatment and is therefore in the domain where semiclassical methods such as FGA-SH have potential application. Combined with the prefactor damping algorithm, the FGA-SH method was able to qualitatively account for the main features in the absorption spectrum with a similar degree of accuracy to that observed with other semiclassical treatments.[**6**] This demonstrates that FGA-SH is a promising method for treating molecules with many degrees of freedom in the nonadiabatic regime.

[1] A. W. Jasper, C. Zhu, S Nangia, D. G. Truhlar, *Faraday Discuss. Chem. Soc* **2004**, *127*, 1-22

[2] K. G. Kay *Chemical Physics*, **2005**, *322*, 3-12

[3] J. Lu, Z. Zhou *Journal of Chemical Physics*, **2016**, *142*, 124109

[4] W. Domcke, A. L. Sobolewski, H. Werner, C. Woywod, *American Institute of Physics* **1993**, *100*,1400-1413

[5] A. Raab, G. A. Worth, H. D. Meyer, L. S. Cederbaum ,*Journal of Chemical Physics* **1999**, *110*, 2, 936

[6] W. H. Miller, G. Stock, M. Thoss, *Journal of Chemical Physics* **2000**, 112, 10282

# Table of Contents

## FINAL HONOUR SCHOOL OF CHEMISTRY

# DECLARATION OF AUTHORSHIP

*This certificate should be completed and submitted with your Part II Thesis by hand at the Examination Schools, addressed to the "Clerk of the Schools, Oxford, for the Chairman of Examiners in Part II of the Final Honour School of Chemistry" not later than noon on Friday of the seventh week of full term.*

**Name (in capitals):** **Candidate number:**

**College (in capitals):** **[Supervisor/Adviser:]**

**Title of thesis (in capitals):**

*Please tick to confirm the following:*

I am aware of the University's disciplinary regulations concerning conduct in examinations and, in particular, of the regulations on plagiarism. ☐

The thesis I am submitting is entirely my own work except where otherwise indicated. ☐

It has not been submitted, either wholly or substantially, for another Honour School or degree of this University, or for a degree at any other institution. ☐

I have clearly signalled the presence of quoted or paraphrased material and referenced all sources. ☐

I have acknowledged appropriately any assistance I have received in addition to that provided by my supervisor. ☐

I have not sought assistance from any professional agency. ☐

I agree to retain an electronic version of the work and to make it available on request from the Chair of Examiners should this be required in order to check for plagiarism.

Candidate's signature: Date:

…………………………………………….. ………………………..

# Acknowledgements

I would like to thank David Manolopoulos for suggesting such an interesting project, and for his ideas along the way. Many thanks go to Joseph Lawrence for diligently proof-reading my thesis and for being extremely supportive over the course of the year, also to Lachlan Lindoy for his mathematical insight and for many helpful tips for fixing bugs in my code.

I would also like to thank my tutors: Richard Compton, Fraser Armstrong and Angela Russell, for the care and effort they have all put into tutorials over the past years, and for the profound enthusiasm with which they all approach the subject.

Lastly, I wish to thank my parents for their constant sense of humour and for putting things into perspective when required.

# Abbreviations

| | |
|---|---|
| a.u | Atomic time unit, $1\text{a.u} = 2.41888 \times 10^{-17}\,\text{s}$ |
| eV | Electron Volt, $1eV = 1.60218 \times 10^{-19}\,\text{J}$ |
| e | Euler's number, $\text{e} = 2.71828\ldots$ |
| $\hbar$ | Reduced Planck Constant, $\frac{h}{2\pi} = 1.0545718 \times 10^{-34} m^2 kg s^{-1}$ |
| fs | femtoseconds |
| nm | nanometers |
| UV | ultraviolet |
| CASSCF | Complete-Active-Space Self-Consistent Field |
| CIS | Single-Excitation Configuration Interaction |
| FGA | Frozen Gaussian Approximation |
| FGA-SH | Frozen Gaussian Approximation with Surface Hopping |
| MCTDH | Multi-Configurational Time Dependent Hartree |
| MP2 | Møller-Plesset |
| TDSE | Time Dependent Schrödinger Equation |

## Chapter 1

# Introduction

Nonadiabatic dynamics is an area for which, at present, no entirely satisfactory computational method exists. In nonadiabatic systems, the electronic and nuclear motion are coupled, which allows non-radiative transitions between the electronic energy levels to occur.[1] In theory, a full description of this process could be obtained by solving the Time Dependent Schrödinger Equation (TDSE) with all of the electronic and nuclear degrees of freedom included. However, the computational time required to perform such calculations for multiple coupled electronic surfaces increases exponentially with the number of nuclear degrees of freedom.[2] As a result, molecules with a large number of electrons and nuclei that exhibit nonadiabatic dynamics cannot be treated by an exact quantum mechanical method.

In many cases, progress can be made through exploiting correspondences between the quantum and classical pictures, allowing a series of approximations to be made that render computation feasible. Such approximations have allowed accurate dynamical simulations to be performed for large systems, such as protein folding[3] and enzymatic catalysis.[4] In the nonadiabatic regime, however, the dynamics that permit a wavefunction to separate onto different electronic surfaces are inherently quantum mechanical. Thus, there is a need for a method that accurately captures the quantum nature of the nonadiabatic regime which is computationally feasible for the systems one wishes to study. In this thesis, we investigate a new semiclassical method for calculating the absorption spectra of molecules where nonadiabatic effects are important.

## 1.1 Adiabatic Dynamics

For many molecules, it is possible to simplify dynamical simulations by using the Born-Oppenheimer approximation. This assumes that the nuclei are sufficiently slow compared to the electrons that they can be considered frozen while the electronic part of the wavefunction is calculated. Although these electronic structure calculations remain a challenging task, a great deal of work has been done to develop methods that tackle the problem. These range in complexity from approximate force-field models to ab-initio Density Functional Theory calculations that take into account exchange interactions[5] and relativistic effects.[6] By incrementing the nuclear coordinates, the electronic energy levels in a system can be determined at each position and a set of uncoupled potential energy surfaces or ‘adiabats’ can be constructed.

The nuclear dynamics on these adiabats often correspond closely to the classical picture. By constructing a Hamiltonian, $\hat{\mathcal{H}} = \frac{\mathbf{p}^2}{2m} + V_l(\mathbf{q})$, where $\mathbf{p}$ is a vector containing the momenta of the nuclei and $V_l(\mathbf{q})$ is the potential of adiabat $l$ at coordinate $\mathbf{q}$, the nuclei can be evolved across the surface classically. This so-called ‘molecular dynamics’ approach rests on the assumption that the nuclei are sufficiently heavy that their evolution is dictated by classical mechanics. Since a description of the system only requires the nuclear positions $\mathbf{q}$ and momenta $\mathbf{p}$, these methods will scale polynomially with the number of atoms in the molecule and thus for large systems will be much faster than finding the nuclear wavefunction from the TDSE.

In thermal condensed phase systems like liquid water, quantum phenomena such as tunnelling and zero point energy can be important, but will not be accounted for by classical molecular dynamics. To treat these systems, Ring Polymer Molecular Dynamics (RPMD) can be employed, which is an approximation to the path integral representation in imaginary time.[7] This evolves the nuclei in an extended phase space and is able to capture these effects. However, RPMD does not account for coherence, which is a result of quantum mechanical interference effects. This is not a problem in simulations of liquid water[8], where any coherence exhibited by a molecule will be largely damped out by the surrounding system.

There are a number of cases where coherence *cannot* be ignored. In the adiabatic regime, this often occurs when the system is not surrounded by a bath, which is the case for small molecules in the gas phase. To accurately model the dynamics in such systems while avoiding the full cost of quantum mechanical evaluation, *semi-classical* methods can be employed. These involve treating the dynamics of the nuclei classically while retaining some of the quantum nature, including phase information critical to a description of coherence. One such method is the Frozen Gaussian Approximation (FGA)[9], which is the focus of this thesis. In FGA, the initial wavefunction is represented in a basis of Gaussian wavepackets. These Gaussian wavepackets are then allowed to evolve classically with their widths frozen, whilst simultaneously accumulating a complex phase factor. At some later time, the wavefunction can thus approximated in the basis of the classically evolved frozen Gaussians. The inclusion of phase information allows the FGA method to accurately predict interference effects.[10]

## 1.2 Nonadiabatic Dynamics

Where adiabatic surfaces come close in energy, the timescales of electronic and nuclear motion become comparable and the Born-Oppenheimer approximation breaks down. The dynamics in such systems are referred to as electronically *nonadiabatic*. As the nuclear wavepacket enters a nonadiabatic region it may bifurcate, dividing into separate components on each of the interacting surfaces. This is difficult to model due to the importance of coherence effects, which are entirely quantum mechanical in origin.

Nonadiabatic dynamics are crucial to the ability of many naturally occurring molecules to non-radiatively convert between electronic states after photoexcitation, as seen for example in the protein responsible for vision rhodopsin[11], the skin pigment melanin[12] and the nucleobases of DNA[13]. After excitation by a photon to a higher electronic state, these molecules rapidly decay back to their ground states, dissipating the additional energy as heat. For the nucleobase uracil, the lifetime of the excited state is just 2.4 picoseconds.[13] Over this short period of time, processes such as heterolytic fission, which generates free radicals that can oxidatively damage genetic material, cannot occur.

Due to the importance of accurately describing these systems, a number of fully quantum mechanical methods have been developed. These methods attempt to simplify the problem by approximating the full quantum mechanical solution to the wavefunction by working in a smaller Hilbert space. Two popular methods, which have been successfully employed in a range of nonadiabatic systems, are the Full Multiple Spawning method (FMS)[14] and the Multi-Configurational Time Dependent Hartree method (MCTDH).[2] In the FMS method, the nuclear wavepacket is represented in a relatively small basis set of Gaussian wavepackets. The basis set is evolved classically across an adiabat, and when a trajectory enters a region of significant coupling to a second adiabat, additional basis states are spawned on the second surface. At any later time, the phase space that the trajectories span will be an approximation to the Hilbert space relevant to the nuclear wavefunction. Therefore, the basis set is expanded only in regions of strong nonadiabatic coupling, so the size of the basis set used to describe the wavefunction is reduced. In MCTDH the size of the basis set is also reduced, by approximating the wavefunction with a variationally optimised set of time-dependent single particle functions. A difficulty encountered with both of these methods is that, although the computational cost is reduced, they still scale exponentially with the number of basis functions required, which may need to span a large fraction of the full Hilbert space if the system under study is chaotic.[2]

As in the adiabatic case, it is desirable to treat the nuclei classically to circumvent the exponential scaling with nuclear coordinates. The difficulty for nonadiabatic systems is to account for the discrete electronic states while retaining the classical nuclear dynamics. There have been two principal approaches to this problem. In the Fewest Switches Surface Hopping (FSSH) method[15], the nuclei are evolved as in conventional adiabatic molecular dynamics. At any point, the degree of coupling between the adiabats is used to determine whether the trajectory hops between the surfaces, which retains their fundamentally discrete nature. However, this method suffers from 'over-coherence': it does not account for uncoupling or decoherence between the nuclear wavepackets on different surfaces, which leads to inaccurate predictions for the long time dynamics.[16]

Another approach is to use a quantum mechanical bosonisation technique, in which the discrete electronic states are mapped onto continuous degrees of freedom, which can then be incorporated into semiclassical dynamics. In an application of this approach, Stock and Thoss mapped the N electronic states onto the degenerate first excited states of an N-dimensional harmonic oscillator and then ran dynamical simulations on the modified system using FGA theory.[17] As phase information is retained in FGA, some coherence effects arising from the nonadiabatic dynamics could be correctly accounted for.

In this thesis a new semiclassical method introduced by Lu and Zhou[18], and derived using rigorous asymptotic analysis, will be tested in a real chemical system for the first time. The method is a generalisation of the Frozen Gaussian Approximation to two (or more) coupled electronic surfaces. In contrast to the mapping variable technique, this theory accounts for the existence of multiple surfaces by employing a surface-hopping algorithm somewhat similar to the FSSH method. As it is an extension of the single surface Frozen Gaussian Approximation which utilises surface hopping, we will refer to this method as the 'Frozen Gaussian Approximation with Surface Hopping' or FGA-SH.

## 1.3 Absorption Spectra and Autocorrelation Functions

In order to test the efficacy of the FGA-SH method, we will focus on simulating Franck-Condon absorption spectra, neglecting any rotational structure. We can write the absorption spectrum $I(E)$ that results from excitation of the ground electronic and vibrational state of a molecule, $|\Psi_0\rangle$, to each of the eigenstates of its excited vibronic manifold, $|\Psi_k\rangle$ as

$$I(E) = \sum_k |\langle\Psi_k|\hat{\mu}|\Psi_0\rangle|^2 \delta(E - E_k) \tag{1.1}$$

where $k$ runs over the vibronic eigenstates that have energies $E_k$, and $\hat{\mu}$ is the dipole moment operator. Equation (1.1) can be alternatively expressed in the form

$$I(E) = \sum_k \langle\Psi_0|\hat{\mu}|\Psi_k\rangle \, \delta(E - E_k) \, \langle\Psi_k|\hat{\mu}|\Psi_0\rangle, \tag{1.2}$$

which is the spectral representation of

$$I(E) = \langle\Phi_0|\delta(E - \hat{\mathcal{H}})|\Phi_0\rangle, \tag{1.3}$$

where

$$|\Phi_0\rangle = \hat{\mu}|\Psi_0\rangle, \tag{1.4}$$

$$\delta(E - \hat{\mathcal{H}}) = \sum_k |\Psi_k\rangle \, \delta(E - E_k) \, \langle\Psi_k|, \tag{1.5}$$

and $\hat{\mathcal{H}}$ is the vibronic Hamiltonian of the excited manifold,

$$\hat{\mathcal{H}} = \sum_k |\Psi_k\rangle \, E_k \, \langle\Psi_k|. \tag{1.6}$$

Using the Fourier representation of Equation (1.5),

$$\delta(E - \hat{\mathcal{H}}) = \frac{1}{2\pi} \int_{-\infty}^{\infty} e^{i(E - \hat{\mathcal{H}})t} dt, \tag{1.7}$$

allows us to write an expression for $I(E)$ in the time domain:

$$I(E) = \frac{1}{2\pi\hbar}\int_{-\infty}^{\infty} e^{\frac{+iEt}{\hbar}} C(t)\mathrm{d}t, \tag{1.8}$$

In Equation (1.8), $C(t)$ is the autocorrelation function, given by

$$C(t) = \langle\Phi_0| e^{\frac{-i\hat{\mathcal{H}}t}{\hbar}} |\Phi_0\rangle \equiv \langle\Phi_0|\Phi_t\rangle, \tag{1.9}$$

where $|\Phi_t\rangle$ satisfies the TDSE,

$$i\hbar\frac{\partial|\Phi_t\rangle}{\partial t} = \hat{\mathcal{H}}|\Phi_t\rangle \tag{1.10}$$

subject to the initial condition $|\Phi_0\rangle = \hat{\mu}|\Psi_0\rangle$ from Equation (1.4). Writing Equation (1.8) in the form,

$$I(E) = \frac{1}{2\pi\hbar}\int_{0}^{\infty} e^{\frac{+iEt}{\hbar}} C(t) + e^{\frac{-iEt}{\hbar}} C(-t)\mathrm{d}t \tag{1.11}$$

and inserting $C(-t) = C^*(-t)$, which is implied by Equation (1.9), we get that

$$I(E) = \frac{1}{\pi\hbar}Re\int_{0}^{\infty} e^{\frac{+iEt}{\hbar}} C(t)\mathrm{d}t \tag{1.12}$$

The advantage of this time dependent formulation of $I(E)$ is that we are now able to solve the TDSE without having to know the eigenstates of $\hat{\mathcal{H}}$. Instead, we are now required to evaluate the autocorrelation function $C(t)$ over a sufficiently long period of time that the limit $t \to \infty$ in Equation (1.12) is obtained. The calculation of $C(t)$ involves propagating the wavepacket $|\Phi_0\rangle$ under the operator $e^{-i\hat{\mathcal{H}}t}$, either in a quantum mechanical basis or, as in this thesis, via a semiclassical approximation. Simulating absorption spectra provides a good test for the validity of new nonadiabatic theories, as their agreement with experiment can be seen as the visual representation of the theory's success in solving the TDSE.

## 1.4 Pyrazine

To test the new semiclassical theory in a real chemical system, we chose to simulate the gas-phase absorption spectrum of pyrazine, shown in Figure 1.1.

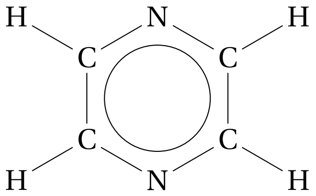

**Figure 1.1** Molecular pyrazine in its equilibrium geometry

This is a benchmark nonadiabatic system that has been simulated by many methods, including FSSH[19], mapping-variable FGA[20] and MCTDH[21] approaches. The challenge in modelling the dynamics of pyrazine is that there exists a conical intersection, depicted in Figure 1.2, between its two lowest singlet excited states, which we will label $S_1$ and $S_2$.

A conical intersection is a particular set of nuclear coordinates for which there is an exact degeneracy between the adiabats. In the vicinity of a conical intersection, there is an increase in the derivative coupling between the surfaces (defined in Chapter 2), which becomes singular at the point of degeneracy.[22] This affects the dynamics by essentially acting as funnel, greatly increasing the speed at which transitions from the higher energy adiabat onto the lower adiabat occur. Conical intersections are common features of molecules with many degrees of nuclear freedom, and although they are often depicted as being located at a single set of nuclear coordinates, they exist in a $3N-8$ dimensional subspace, where $N$ is the number of atoms in the molecule.[23] As a result of the extensive vibronic coupling in pyrazine, the region of the spectrum originating from excitation to the $S_2$ surface is much more congested than it would otherwise be, with a distinctive diffuse structure.

In order to simulate the spectrum, it has been shown that one only needs to consider the two lowest electronically excited states, $S_1$ and $S_2$.[25] Since they are separated from $S_0$, the ground electronic state, by a large energy gap of more than 4eV,

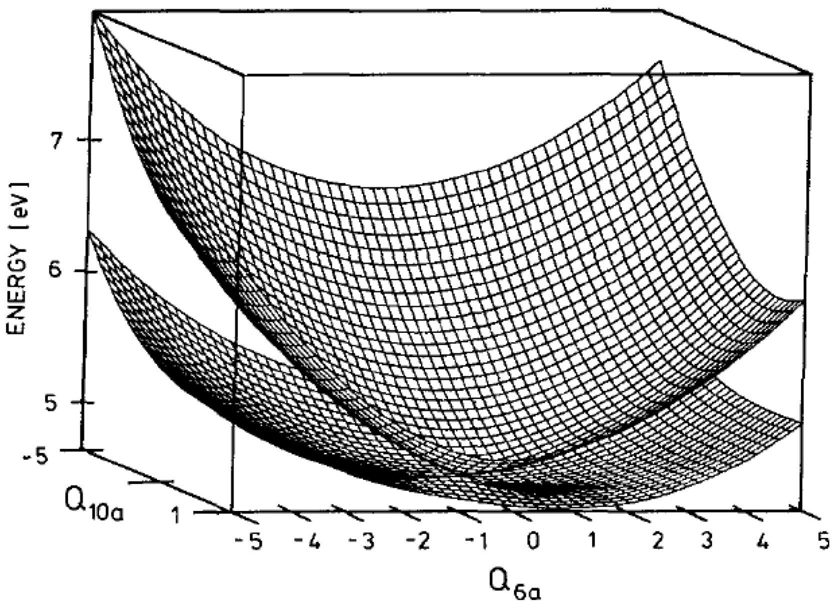

**Figure 1.2** Plot of the energies of the $S_1$ and $S_2$ electronic states in pyrazine as a function of two of the vibrational normal modes, revealing the conical intersection. Taken from calculations performed by Woywod et al.[24]

the $S_0 - S_1$ or $S_0 - S_2$ coupling elements are negligibly small. This means that for the purpose of simulating its absorption spectrum, pyrazine can be considered a two-state system in which, after photoexcitation, the nuclear wavepacket evolves only on the $S_1$ and $S_2$ surfaces.[24]

### 1.4.1 Experimental Spectra

The gas phase absorption spectrum of pyrazine has been obtained experimentally using Picosecond Time-Resolved Fluorescence Spectroscopy.[26] It has two distinct regions located in the near ultraviolet range, whose features correspond to excitation to the vibrational states in the $S_1 - S_2$ manifold. The first region of the spectrum, reproduced in Figure 1.3, is a band of lower energy transitions from 300 nm to 325 nm. These energies are close to the vertical excitation energy $S_0 \rightarrow S_1$. This region will therefore be referred to as the '$S_1$ region'.

The second region, Figure 1.4, is a band of higher energy transitions from 220 nm to 290 nm and will be referred to as the '$S_2$ region'. From the relative intensities, it can be noted that this is the dominant feature of the spectrum. Its line width is the result of many unresolved vibrational peaks in this energy range which come from the extensive mixing of the adiabats around the conical intersection.[24]

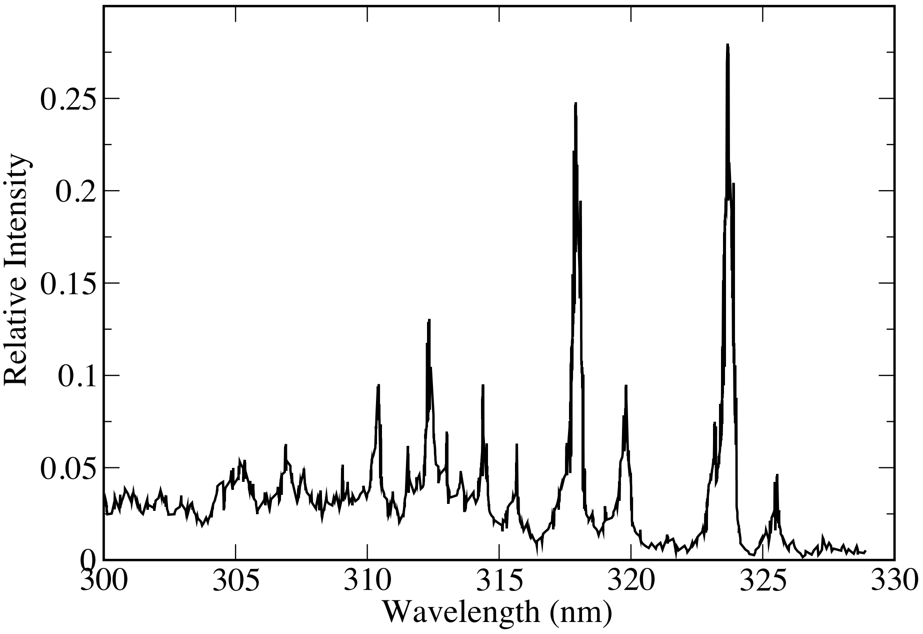

**Figure 1.3** The $S_1$ region of the experimental absorption spectrum of pyrazine[26]

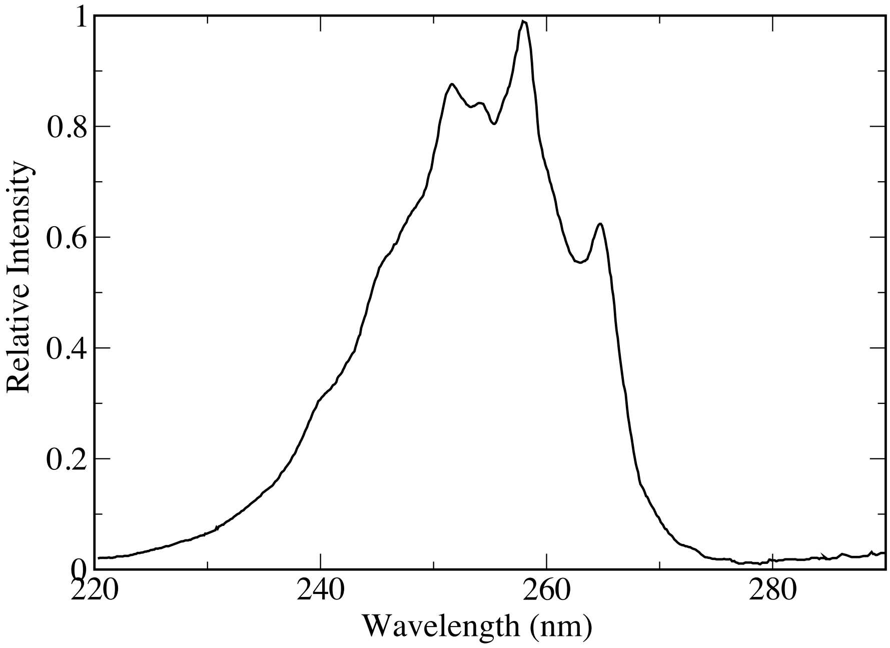

**Figure 1.4** The $S_2$ region of the experimental absorption spectrum of pyrazine[26]

### 1.4.2 Symmetry

In its ground state equilibrium geometry, pyrazine is a member of the $D_{2h}$ point group. Defining the axes with $z$ intersecting the nitrogen atoms and $x$ perpendicular to the plane of the molecule, the $S_1$ electronic state, which is $[n\pi^*]$, has $B_{3u}$ symmetry and $S_2$, which is $[\pi\pi^*]$, has $B_{2u}$ symmetry. To find the symmetries of the vibrational normal modes, we first write the irreducible representation spanned by all ten nuclei $(2 \times N + 4 \times H + 4 \times C)$ in the $D_{2h}$ group:

$$\Gamma_{tot} = 5\Gamma_{A_g} \oplus 2\Gamma_{B_{1g}} \oplus 3\Gamma_{B_{2g}} \oplus 5\Gamma_{B_{3g}} \oplus 2\Gamma_{A_u} \oplus 5\Gamma_{B_{1u}} \oplus 5\Gamma_{B_{2u}} \oplus 3\Gamma_{B_{3u}}. \tag{1.13}$$

Then, to find $\Gamma_{vib}$, we use the fact that $\Gamma_{vib} = \Gamma_{tot} - \Gamma_{trans} - \Gamma_{rot}$, where

$$\Gamma_{trans} = \Gamma_x \oplus \Gamma_y \oplus \Gamma_z = \Gamma_{B_{1u}} \oplus \Gamma_{B_{2u}} \oplus \Gamma_{B_{3u}}, \tag{1.14}$$

$$\Gamma_{rot} = \Gamma_{R_x} \oplus \Gamma_{R_y} \oplus \Gamma_{R_z} = \Gamma_{B_{1g}} \oplus \Gamma_{B_{2g}} \oplus \Gamma_{B_{3g}}, \tag{1.15}$$

which gives the 24 vibrational normal modes in pyrazine,

$$\Gamma_{vib} = 5\Gamma_{A_g} \oplus \Gamma_{B_{1g}} \oplus 2\Gamma_{B_{2g}} \oplus 4\Gamma_{B_{3g}} \oplus 2\Gamma_{A_u} \oplus 4\Gamma_{B_{1u}} \oplus 4\Gamma_{B_{2u}} \oplus 2\Gamma_{B_{3u}}, \tag{1.16}$$

## 1.5 Outline of Thesis

Chapter 2 introduces the Frozen Gaussian Approximation first for single surfaces and then with the stochastic surface hopping algorithm for nonadiabatic systems with two or more coupled electronic states. In Chapter 3, we derive an expression for the autocorrelation function, and provide an efficient procedure for simulation. Chapter 4 applies this method to the reduced 4-mode model of pyrazine and compares the resulting absorption spectra to exact quantum mechanical simulations. This is expanded to the full 24-mode pyrazine molecule in Chapter 5, where the method is compared to MCTDH simulations. Chapter 6 concludes the thesis.

## Chapter 2

# Theory

In this chapter, we begin with a general discussion of semiclassical approximations and their relation to the path integral formulation of quantum mechanics. Following this, we introduce the Frozen Gaussian Approximation for single surface dynamics, which provides a great deal of the theoretical basis behind FGA-SH, its multiple surface extension. We then move on to the focus of this thesis, nonadiabatic dynamics. By formulating the problem of coupled electronic surfaces in terms of the nonadiabatic Schrödinger Equation, we build a framework on which to develop and understand the FGA-SH expression.

## 2.1 The Semiclassical Approximation

In classical mechanics, the dynamics of a system can be represented by a path taken through space, points on which are represented by the position vector, $\mathbf{q}(t)$, which has a dimension $N$, the number of nuclear degrees of freedom in the system. The route taken from $t = 0$ until some later point, $t = t'$, determines the value of the action, $S[\mathbf{q}](t')$, a functional of $\mathbf{q}(t)$, which is given by:

$$S[\mathbf{q}](t') = \int_0^{t'} T(\dot{\mathbf{q}}(t)) - V(\mathbf{q}(t))\mathrm{d}t, \tag{2.1}$$

where $T(\dot{\mathbf{q}}(t))$ and $V(\mathbf{q}(t))$ are the kinetic and potential energies respectively. The principle of least action[27] states that the action for classical system, $S_c$, satisfies

$$\frac{\delta S_c[\mathbf{q}]}{\delta \mathbf{q}(t)} = 0, \tag{2.2}$$

meaning that the path taken by a classical system will be that for which the action is stationary with respect to small changes in the position, $\delta\mathbf{q}(t)$.

In the path integral formulation of quantum mechanics introduced by Richard Feynman,[28] the dynamics of a system can be related to a sum over an infinite number of paths that start at $\mathbf{q}_0$ and arrive at $\mathbf{q}_t$ at time $t$. Each path contributes a complex probability amplitude proportional to $\exp(\frac{iS}{\hbar})$.[28] Taking the square modulus of the total probability amplitude, the probability that at time $t$ the system is located at $\mathbf{q}_t$ may be determined.

The non-classical paths that do not satisfy Equation (2.2) are those for which the value of the action will change on a small perturbation to the path, $\delta\mathbf{q}(t)$. These non-classical paths will have different values of $S$, so each of their contributions to the total probability amplitude ,$\exp(\frac{iS}{\hbar})$, will have different phases. A sum over these non-classical paths will thus be approximately zero, as their phases will tend to destructively cancel each other. Therefore, it is possible to employ the stationary phase approximation, which states that only paths that are close to the classical path need to be considered.[29] Neglecting the remaining paths becomes valid in the limit that $\hbar \rightarrow 0$ as here only the classical stationary points contribute. Semiclassical methods take this limit to derive expressions that account for quantum behaviour by including oscillatory paths to some order in $\hbar$.

## 2.2 The Adiabatic Frozen Gaussian Approximation

The Frozen Gaussian Approximation (FGA), developed by Herman and Kluk[30], is a semiclassical method that gives a solution $|\Psi_t\rangle$, correct to order $\hbar$, of the Time Dependent Schrödinger Equation for one surface,

$$|\Psi_t\rangle = e^{-\frac{i\hat{\mathcal{H}}t}{\hbar}}|\Psi_0\rangle \tag{2.3}$$

The theory is rigorously semiclassical in the sense that it provides a uniform approximation to $|\Psi_t\rangle$ that is free from caustic singularities.[31]

In this thesis we will be considering systems that, at $t = 0$, have an initial wavefunction that is an $N$ dimensional Gaussian wavepacket centred around $(\mathbf{p}_i, \mathbf{q}_i)$. We express this wavefunction, $|\Psi_0\rangle$ in the position representation as

$$\langle \mathbf{x}|\Psi_0\rangle = \left(\frac{\det(\boldsymbol{\gamma})}{\pi}\right)^{\frac{N}{4}} \exp(-\frac{1}{2}(\mathbf{x}-\mathbf{q}_i)^{\mathsf{T}}\boldsymbol{\gamma}(\mathbf{x}-\mathbf{q}_i) - \frac{i}{\hbar}\mathbf{p}_i^{\mathsf{T}}(\mathbf{x}-\mathbf{q}_i)). \tag{2.4}$$

where $\boldsymbol{\gamma}$ is a diagonal $N \times N$ width matrix with elements related to the angular frequencies, $\boldsymbol{\gamma}_{ii} = \frac{m\omega_i}{\hbar}$. In this thesis, we will work in a coordinate system in which $\boldsymbol{\gamma} = \hat{\mathbf{1}}$, so that the wavefunction can be written more simply as

$$\langle \mathbf{x}|\Psi_0\rangle = \left(\frac{1}{\pi}\right)^{\frac{N}{4}} \exp(-\frac{1}{2}(\mathbf{x}-\mathbf{q}_i)^2 - \frac{i}{\hbar}\mathbf{p}_i \cdot (\mathbf{x}-\mathbf{q}_i)). \tag{2.5}$$

This initial wavefunction is equivalent to $|g_{\mathbf{p}_i\mathbf{q}_i}\rangle$ where $|g_{\mathbf{pq}}\rangle$ denotes a coherent state of a harmonic oscillator centred at $(\mathbf{p}, \mathbf{q})$ with the same width as the initial wavefunction. Coherent states are defined as the eigenvectors of the annihilation operator, $\hat{a}$, and have the property of being Gaussians in phase space with a constant width at all times.[32]

To derive the FGA expression, we first write the identity operator in the coherent state representation:

$$\hat{1} = \left(\frac{1}{2\pi\hbar}\right)^{N} \int d^N\mathbf{p}_0 \int d^N\mathbf{q}_0 \, |g_{\mathbf{p}_0\mathbf{q}_0}\rangle\langle g_{\mathbf{p}_0\mathbf{q}_0}|. \tag{2.6}$$

and on inserting Equation (2.6) into Equation (2.3), we get that

$$|\Psi_t\rangle = \left(\frac{1}{2\pi\hbar}\right)^{N} \int d^N\mathbf{p}_0 \int d^N\mathbf{q}_0 e^{-\frac{i\hat{\mathcal{H}}}{\hbar}} |g_{\mathbf{p}_0\mathbf{q}_0}\rangle \langle g_{\mathbf{p}_0\mathbf{q}_0}|\Psi_0\rangle \tag{2.7}$$

The key step in the derivation is to choose to express the time propagated coherent state, $e^{-\frac{i\hat{\mathcal{H}}t}{\hbar}}|g_{\mathbf{p}_0\mathbf{q}_0}\rangle$, in terms of another coherent state, $K_t|g_{\mathbf{p}_t\mathbf{q}_t}\rangle$, where $\mathbf{p}_t$ and $\mathbf{q}_t$ are the position and momentum coordinates obtained by classical evolution over the potential surface starting at ($\mathbf{p}_0$,$\mathbf{q}_0$) up to time $t$, and $K_t$ is an as yet undetermined complex prefactor. Thus, the expression for $|\Psi_t\rangle$ is

$$|\Psi_t\rangle = \left(\frac{1}{2\pi\hbar}\right)^N \int d^N\mathbf{p}_0 \int d^N\mathbf{q}_0 K_t |g_{\mathbf{p}_t\mathbf{q}_t}\rangle\langle g_{\mathbf{p}_0\mathbf{q}_0}|\Psi_0\rangle. \tag{2.8}$$

At $t = 0$, Equation (2.8) must reduce to the initial wavefunction $|\Psi_0\rangle$, which gives us that $K_0 = 1$. However, an analytic expression for $K_t$ at later time is not available. By matching the terms that appear in Equation (2.8) to the solution from the Time Dependent Schrodinger Equation, an expression for $K_t$ can be derived which gives an approximation to $|\Psi_t\rangle$ correct to order $\hbar$.[31] This is the Frozen Gaussian Approximation which is given by

$$\langle\mathbf{x}|\Psi_t\rangle = \frac{1}{(2\pi\hbar)^N} \int d^N\mathbf{p}_0 \int d^N\mathbf{q}_0 R(t) e^{\frac{iS(t)}{\hbar}} \langle\mathbf{x}|g_{\mathbf{p}_t\mathbf{q}_t}\rangle\langle g_{\mathbf{p}_0\mathbf{q}_0}|\Psi_0\rangle. \tag{2.9}$$

From Equation (2.9), it can be seen that $K_t$ comprises two terms: a complex prefactor, $R(t)$, and an additional phase, $e^{\frac{iS(t)}{\hbar}}$. $R(t)$, the 'Hermann-Kluk' prefactor, is a complex number whose value may be calculated from

$$R(t) = \sqrt{\det\left(\frac{1}{2}(\mathbf{M_{pp}} + \mathbf{M_{qq}} - i\mathbf{M_{qp}} + i\mathbf{M_{pq}})\right)}, \tag{2.10}$$

where $\mathbf{M}$ is the monodromy matrix,

$$\mathbf{M} = \begin{pmatrix} \mathbf{M_{pp}} & \mathbf{M_{pq}} \\ \mathbf{M_{qp}} & \mathbf{M_{qq}} \end{pmatrix} = \begin{pmatrix} \frac{\partial\mathbf{p}_t}{\partial\mathbf{p}_0} & \frac{\partial\mathbf{p}_t}{\partial\mathbf{q}_0} \\ \frac{\partial\mathbf{q}_t}{\partial\mathbf{p}_0} & \frac{\partial\mathbf{q}_t}{\partial\mathbf{q}_0} \end{pmatrix}. \tag{2.11}$$

The phase factor, $e^{\frac{iS(t)}{\hbar}}$ depends on the classical action, $S(t)$, which may be calculated using Equation (2.1), with $\dot{\mathbf{q}}(t) = \mathbf{m}^{-1}\mathbf{p}(t)$, where $\mathbf{m}$ is the mass matrix.

The term $\langle g_{\mathbf{p}_0\mathbf{q}_0}|\Psi_0\rangle$ is the overlap of the frozen Gaussian wavepacket at $t = 0$ with the initial wavefunction,

$$\langle g_{\mathbf{p}_0\mathbf{q}_0}|\Psi_0\rangle = \int \mathrm{d}^N\mathbf{x}\,\langle\Psi_0|\mathbf{x}\rangle\,\langle\mathbf{x}|g_{\mathbf{p}_0\mathbf{q}_0}\rangle\,. \tag{2.12}$$

As we have assumed that the initial wavefunction is Gaussian distributed in (2.5), Equation (2.12) may be integrated analytically to give

$$\langle g_{\mathbf{p}_0\mathbf{q}_0}|\Psi_0\rangle = \exp\left(-\frac{1}{4}(\mathbf{q}_0-\mathbf{q}_i)^2 - \frac{1}{4\hbar^2}(\mathbf{p}_0-\mathbf{p}_i)^2 - \frac{i}{2\hbar}(\mathbf{p}_0+\mathbf{p}_i)\cdot(\mathbf{q}_0-\mathbf{q}_i)\right). \tag{2.13}$$

### 2.2.1 Autocorrelation Function

The autocorrelation function can be determined from

$$C(t) = \int \mathrm{d}^N\mathbf{x}\,\langle\Psi_0|\mathbf{x}\rangle\,\langle\mathbf{x}|\Psi_t\rangle, \tag{2.14}$$

so, from Equation (2.8), we get

$$C(t) = \frac{1}{(2\pi\hbar)^N}\int d^N\mathbf{p}_0\int d^N\mathbf{q}_0 R(t)e^{\frac{iS(t)}{\hbar}}\,\langle\Psi_0|g_{\mathbf{p}_t\mathbf{q}_t}\rangle\,\langle g_{\mathbf{p}_0\mathbf{q}_0}|\Psi_0\rangle\,. \tag{2.15}$$

We can choose to take, $\mathbb{P}_{\mathbf{p}_0,\mathbf{q}_0} = \frac{1}{(2\pi\hbar)^N}|\langle g_{\mathbf{p}_0\mathbf{q}_0}|\Psi_0\rangle|^2$ out as a factor from Equation (2.15), which has the form of a Gaussian centred on $(\mathbf{p}_i,\mathbf{q}_i)$:

$$\mathbb{P}_{\mathbf{p}_0,\mathbf{q}_0} = \frac{1}{(2\pi\hbar)^N}\exp\left(-\frac{1}{2}(\mathbf{q}_0-\mathbf{q}_i)^2\right)\times\exp\left(-\frac{(\mathbf{p}_0-\mathbf{p}_i)^2}{2\hbar^2}\right). \tag{2.16}$$

$\mathbb{P}_{\mathbf{p}_0,\mathbf{q}_0}$ is a probability distribution from which initial points in $(\mathbf{p}_0,\mathbf{q}_0)$ space may be chosen, with the necessary property for a probability distribution that,

$$\int d^N\mathbf{p}_0\int d^N\mathbf{q}_0\mathbb{P}_{\mathbf{p}_0,\mathbf{q}_0} = 1 \tag{2.17}$$

Equation (2.15) thus becomes

$$C(t) = \int d^N\mathbf{p}_0 \int d^N\mathbf{q}_0 \mathbb{P}_{\mathbf{p}_0,\mathbf{q}_0} R(t) e^{\frac{iS(t)}{\hbar}} \frac{\langle \Psi_0 | g_{\mathbf{p}_t\mathbf{q}_t} \rangle}{\langle \Psi_0 | g_{\mathbf{p}_0\mathbf{q}_0} \rangle}. \tag{2.18}$$

This can be solved by the Monte-Carlo method. A number of trajectories are started with initial positions and momenta $(\mathbf{p}_0, \mathbf{q}_0)$ sampled from $\mathbb{P}_{\mathbf{p}_0,\mathbf{q}_0}$. They are then evolved over the potential surface classically, allowing $R(t)$ and $S(t)$ to be determined for each trajectory. $C(t)$ can then be calculated by averaging over all of their contributions at time $t$. Evaluation of Equation (2.18) is exact for just one trajectory in the limit that $t \to 0$, where it can be seen that $C(0) = 1$. At $t > 0$, a sufficiently large number of trajectories must be averaged over in order to converge to the correct value. Equation (2.18) has been successfully employed in a number of single surface problems where quantum mechanical effects are important, including the absorption spectrum of $CO_2$[33] and the photodissociation of anionic clusters with up to 15 nuclear degrees of freedom.[34]

## 2.3 The Nonadiabatic Schrödinger Equation

We now turn to the problem of two or more coupled electronic states. Starting with the Time Dependent Schrödinger Equation, we write the Hamiltonian as a sum of two parts, the coupled electronic Hamiltonian $\hat{H}_e$ and the nuclear kinetic energy operator $\hat{T}_n$.

$$i\hbar \frac{\partial \Psi(\mathbf{x}, \mathbf{r}, t)}{\partial t} = \hat{H}\Psi(\mathbf{x}, \mathbf{r}, t) = \left(\hat{H}_e + \hat{T}_n\right)\Psi(\mathbf{x}, \mathbf{r}, t) \tag{2.19}$$

We also choose to write the total wavefunction as a sum over the adiabatic electronic states using the Born-Huang expansion[35]

$$\Psi(\mathbf{q}, \mathbf{r}, t) = \sum_k \phi_k(\mathbf{x}, t)\chi_k(\mathbf{r}; \mathbf{x}). \tag{2.20}$$

In this expression, $\phi_k(\mathbf{x}, t)$ is the nuclear part of the wavefunction on adiabat $k$ at time $t$, which depends on the positions of the nuclei, $\mathbf{x}$, but is independent of the electronic coordinates, $\mathbf{r}$, and $\chi_k(\mathbf{r};\mathbf{x})$ is the usual Born Oppenheimer electronic wavefunction for adiabat $k$ which is a function of the electronic coordinates and depends parametrically on the positions of the nuclei. $\chi_k(\mathbf{r};\mathbf{x})$ is an eigenvector of $\hat{H}_e$, with eigenvalue $E_k(\mathbf{x})$. Substituting this expression for the wavefunction into Equation (2.19), we get

$$\hat{H}\Psi(\mathbf{x},\mathbf{r},t) = \sum_k (E_k(\mathbf{x}) + \hat{T}_n)\phi_k(\mathbf{x},t)\chi_k(\mathbf{r};\mathbf{x}). \tag{2.21}$$

Now, using the fact that $\hat{T}_n = \frac{1}{2}\hat{\mathbf{p}}^\top \mathbf{m}^{-1}\hat{\mathbf{p}} = -\frac{\hbar^2}{2}\nabla_\mathbf{x}^\top \mathbf{m}^{-1}\nabla_\mathbf{x}$, where $\mathbf{m}$ is the diagonal mass matrix, we can operate the nuclear kinetic energy on both the nuclear and electronic wavefunctions. Premultiplying the resulting expression with the orthonormal electronic wavefunction $\chi_j^*(\mathbf{r};\mathbf{x})$ and integrating over the electronic coordinates, $\mathbf{r}$, we get

$$\int \mathrm{d}\mathbf{r}\,\chi_j^*(\mathbf{r};\mathbf{x})\hat{H}\Psi(\mathbf{x},\mathbf{r},t) = \sum_k \left(\delta_{jk}E_k(\mathbf{x}) + \delta_{jk}\hat{T}_n - i\hbar\mathbf{p}^\top\mathbf{m}^{-1}\mathbf{d}_{jk} - \frac{\hbar^2}{2}D_{jk}\right)\phi_k(\mathbf{x},t) \tag{2.22}$$

where $\mathbf{d}_{jk}$ is the derivative coupling between adiabats $j$ and $k$,

$$\mathbf{d}_{jk} = \int \mathrm{d}\mathbf{r}\,\chi_j^*(\mathbf{r};\mathbf{x})\nabla_\mathbf{x}\chi_k(\mathbf{r};\mathbf{x}) \tag{2.23}$$

and $D_{jk}$ is the second derivative coupling,

$$D_{jk} = \int \mathrm{d}\mathbf{r}\,\chi_j^*(\mathbf{r};\mathbf{x})\nabla_\mathbf{x}^\top\mathbf{m}^{-1}\nabla_\mathbf{x}\chi_k(\mathbf{r};\mathbf{x}). \tag{2.24}$$

Taking Equation (2.19) and similarly premultiplying by $\chi_j^*(\mathbf{r};\mathbf{x})$ followed by integration over $\mathbf{r}$, we also have that

$$i\hbar\int \mathrm{d}\mathbf{r}\chi_j^*(\mathbf{r};\mathbf{x})\frac{\partial\Psi(\mathbf{x},\mathbf{r},t)}{\partial t} = i\hbar\dot{\phi}_j(\mathbf{x},t), \tag{2.25}$$

so that equating Equations (2.25) and (2.22) we get

$$i\hbar\dot{\phi}_j(\mathbf{x},t) = \sum_k \left(\delta_{jk}E_k(\mathbf{x}) + \delta_{jk}\hat{T}_n - i\hbar\mathbf{p}^\top\mathbf{m}^{-1}\mathbf{d}_{jk} - \frac{\hbar^2}{2}D_{jk}\right)\phi_k(\mathbf{x},t). \tag{2.26}$$

This is the Equation of motion for the component of the nuclear wavefunction on the $j^{th}$ adiabat.

## 2.4 Semiclassical Solution for Multiple Surfaces

Recently, Lu and Zhou have extended the Frozen Gaussian Approximation to systems with more than one electronic surface.[18] Starting with Equation (2.26), they were able to derive a semiclassical approximation for the elements $\phi_k(\mathbf{x},t)$ accurate to order $\hbar$. For a system with two electronic surfaces, the expression for $\phi_k(\mathbf{x},t) \equiv \langle \mathbf{x} | \phi_t^k \rangle$, is

$$\begin{aligned}\langle \mathbf{x} | \phi_t^k \rangle = &\frac{1}{(2\pi\hbar)^N} \sum_{n=0}^{\infty} \sum_{k_0=1}^{2} \delta_{k,k_n} \int_0^t \mathrm{d}t_n \int_0^{t_n} \mathrm{d}t_{n-1} \ldots \int_0^{t_2} \mathrm{d}t_1 \int \mathrm{d}^N\mathbf{p}_0 \int \mathrm{d}^N\mathbf{q}_0 R(\mathbf{z}_n,t) e^{\frac{iS(\mathbf{z}_n,t)}{\hbar}} \\ &\times \langle \mathbf{x} | g_{\mathbf{p}_t\mathbf{q}_t} \rangle \langle g_{\mathbf{p}_0\mathbf{q}_0} | \phi_0^{k_0} \rangle \prod_{h=1}^{n} \tau^{k_h k_{h-1}}.\end{aligned} \tag{2.27}$$

In this expression, the wavefunction is represented as an integral over trajectories beginning at $(\mathbf{p}_0, \mathbf{q}_0)$ on adiabatic state $k_0$, that undergo $n$ discrete hops between the adiabats at times $0 \le t_1 \le t_2 \le \ldots \le t_n$. The first $n$ integrals in Equation (2.27) account for all possible ordered hopping times. For a given initial condition and set of hopping times, $\mathbf{z}_n = (\mathbf{q}_0, \mathbf{p}_0, k_0, t_1 \ldots t_n)$, the variables $\mathbf{q}_t$, $\mathbf{p}_t$, $R(\mathbf{z}_n,t)$ and $S(\mathbf{z}_n,t)$ are evolved classically between hopping times $t_i$ and $t_{i+1}$, as in the single surface case, over the current adiabat, $k_i$. Thus, the prefactor and action are functions not only of $(\mathbf{p}_0, \mathbf{q}_0)$ and $(\mathbf{p}_t, \mathbf{q}_t)$, but also of all the hopping times, which change the surface along which the quantities are evaluated. At each hop, $h$, the integral in Equation

(2.27) picks up a factor of

$$\tau^{k_h,k_{h-1}} = -\mathbf{p}_{t_h} \cdot \mathbf{d}_{k_h k_{h-1}}(\mathbf{q}_{t_h}) \tag{2.28}$$

where $k_h$ and $k_{h-1}$ denote the adiabat before and after the hop respectively. The inclusion of the Kroenecker delta, $\delta_{k\,k_n}$ in Equation (2.27), ensures that only those trajectories that after $n$ hops have arrived on the $k^{th}$ surface contribute to $\left|\phi_t^k\right\rangle$.

In order to evaluate the integral over all possible hops, Lu and Zhou chose to employ a stochastic surface-hopping algorithm.[36] This involves running a large number of trajectories, each of which, from the probabilistic nature of the hopping criterion, will have different hopping times $0 \leq t_1 \leq t_2 \leq \ldots \leq t_n$. An average over all trajectories will thus approximate the integral for a sufficiently large sample size. This technique bares some resemblance to that employed in Tully's 'Fewest Switches Surface Hopping' (FSSH).[15] However, whereas in FSSH, the probability that a hop occurs between time $t$ and $t+\mathrm{d}t$ is decided based on an equation that makes reference to the surface populations, surface hopping in this method is decided by a rate, $\lambda$, which is derived directly from the semiclassical treatment of Equation (2.26)[36], and is given by

$$\lambda = \left|\tau^{3-k,k}\right| \mathrm{d}t, \tag{2.29}$$

where $k$ denotes the current surface and $3-k$ is the other surface, (i.e. for $k=1,\ 3-k=2$ and vice versa). Whereas in FSSH the momentum of a trajectory is adjusted after a hop so as to conserve energy, in FGA-SH, this is not necessary, as we are concerned only with the ensemble properties of the trajectories.[36]

Allowing the system to stochastically hop between surfaces following a probability determined by Equation (2.29) will not correctly sample the integral in Equation (2.27), because a series of hops determined by $\lambda$ will follow a Poisson distribution through time, instead of evenly sampling over all times as required. This distribution will be non-uniform in time due to the variation of $\tau$ for each trajectory. The probability of making $n$ hops, with hopping rate $\lambda$ is given by

$$P(n) = \int_0^t \mathrm{d}t_n \int_0^{t_n} \mathrm{d}t_{n-1} \ldots \int_0^{t_2} \mathrm{d}t_1 e^{-\omega(t)} \prod_{h=1}^{n} \left|\tau^{k_n,k_{n-1}}\right| \tag{2.30}$$

where

$$\omega(t) = \int_0^t |\tau(t')| \mathrm{d}t'. \tag{2.31}$$

for the piecewise function

$$\tau(t) = \tau^{3-k_h,k_h} \qquad , \qquad t_h < t < t_{h+1} \tag{2.32}$$

The probability density for a particular sequence of hops will be

$$\rho(t_1, t_2 \ldots t_n) = \frac{1}{P(n)} e^{-\omega(t)} \prod_{h=1}^{n} \left|\tau^{k_n,k_{n-1}}\right|, \tag{2.33}$$

and therefore, the probability of a particular hopping sequence happening in the stochastic algorithm will be $P(n) \times \rho(t_1, t_2 \ldots t_n)$. Multiplying Equation (2.27) through by $\frac{P(n)\rho(t_1,t_2\ldots t_n)}{P(n)\rho(t_1,t_2\ldots t_n)}$, we get that

$$\begin{aligned}\left\langle \mathbf{x} \middle| \phi_t^k \right\rangle = &\frac{1}{(2\pi\hbar)^N} \sum_{n=0}^{\infty} \sum_{k_0=1}^{2} \delta_{k,k_n} \int_0^t \mathrm{d}t_n \int_0^{t_n} \mathrm{d}t_{n-1} \ldots \int_0^{t_2} \mathrm{d}t_1 \int \mathrm{d}^N \mathbf{p}_0 \int \mathrm{d}^N \mathbf{q}_0 P(n) \rho(t_1, t_2 \ldots t_n) \\ &\times R(\mathbf{z}_n, t) e^{\frac{iS(\mathbf{z}_n,t)}{\hbar}} \langle \mathbf{x} | g_{\mathbf{p}_t \mathbf{q}_t} \rangle \left\langle g_{\mathbf{p}_0 \mathbf{q}_0} \middle| \phi_0^{k_0} \right\rangle e^{\omega(t)} \prod_{h=1}^{n} \frac{\tau^{k_h,k_{h-1}}}{\left|\tau^{k_h,k_{h-1}}\right|}.\end{aligned} \tag{2.34}$$

This integral over $P(n)\rho(t_1, t_2 \ldots t_n)$ is now exactly the inhomogeneous distribution that will arise from the stochastic hopping algorithm. Because of its similarities to both the Frozen Gaussian Approximation and surface hopping methods, this theory will be referred to as 'Frozen Gaussian Approximation with Surface Hopping' or FGA-SH. No reference is made to the second derivative coupling matrix, $\mathbf{D}$ in the FGA-SH expression. This is because the only term that it appears in Equation (2.26) is second order in $\hbar$, so it is neglected in making a semiclassical approximation to $\mathcal{O}(\hbar)$.

## Chapter 3

# Implementation

In this chapter, we show how the FGA-SH method derived in Chapter 2 can be implemented to obtain gas-phase absorption spectra for molecules with two coupled electronic surfaces. As detailed in section 1.3, in order to do this we must simulate the autocorrelation function, $C(t)$, which is given by the overlap of the wavefunction at time $t$ onto itself at $t = 0$, the point immediately after excitation. $C(t)$ must be calculated for a time period that is sufficiently long to converge the absorption spectrum, which is the Fourier transform of $C(t)$.

In order to calculate the autocorrelation function, we first need to find the form of the initial wavefunction, $\Psi(\mathbf{x}, \mathbf{r}, t)$. Although FGA-SH theory could be applied to higher temperatures, where the system begins in a linear combination of excited vibrational states, we choose to work at 0 Kelvin to simplify the problem. This means that, before excitation, the molecule will be in the lowest energy vibrational and electronic levels.

As is typical for the field, the models we assume that for small perturbations in the nuclear geometry, the system is approximately harmonic. As such, the initial wavepacket will be the ground state solution for a harmonic oscillator, i.e. a Gaussian function in position, centred at the equilibrium geometry, $(\mathbf{q}_i, \mathbf{p}_i) = (0, 0)$. In this work, we make the Condon approximation in the adiabatic basis, which assumes that the transition dipole moment for the electronic transition is independent of the nuclear geometry. Hence the form of the initial wavefunction is a product of a Gaussian in the nuclear coordinates, $\phi_k(\mathbf{x}, 0)$ and a single adiabatic electronic state $\chi_k(\mathbf{r}; \mathbf{x})$.

## 3.1 Adiabatic Autocorrelation Function

As in section 2.2, the initial wavefunction after excitation to adiabat $k$, can be written as a product of its nuclear and electronic parts,

$$\Psi_k(\mathbf{x},\mathbf{r},0) = \phi_k(\mathbf{x},0)\chi_k(\mathbf{r};\mathbf{x}). \tag{3.1}$$

The adiabatic autocorrelation function is given by

$$\begin{aligned} C_k(t) &= \int \mathrm{d}\mathbf{r} \int \mathrm{d}\mathbf{x}\phi_k^*(\mathbf{x},0)\chi_k(\mathbf{r};\mathbf{x})\phi_k(\mathbf{x},t)\chi_k(\mathbf{r};\mathbf{x}) \\ &= \int \mathrm{d}\mathbf{x}\phi_k^*(\mathbf{x},0)\phi_k(\mathbf{x},t) \\ &\equiv \left\langle \phi_0^k \middle| \phi_t^k \right\rangle, \end{aligned} \tag{3.2}$$

where we have used the orthonormality of the electronic states,

$$\int \mathrm{d}\mathbf{r}\chi_l^*(\mathbf{r};\mathbf{x})\chi_k(\mathbf{r};\mathbf{x}) = \delta_{lk}. \tag{3.3}$$

Now, inserting the FGA-SH expression for $\left|\phi_t^k\right\rangle$ from equation (2.34), we arrive at an expression for the adiabatic autocorrelation function,

$$\begin{aligned} C_k(t) = &\frac{1}{(2\pi\hbar)^N}\sum_{n=0}^{\infty}\delta_{kk_n}\int_0^t \mathrm{d}t_n \int_0^{t_n} \mathrm{d}t_{n-1}\ldots\int_0^{t_2} \mathrm{d}t_1 \int \mathrm{d}^N\mathbf{p}_0 \int \mathrm{d}^N\mathbf{q}_0 P(n)\rho(t_1,t_2\ldots t_n) \\ &\times R(\mathbf{z}_n,t)e^{\frac{iS(\mathbf{z}_n,t)}{\hbar}}\left\langle \phi_0^k \middle| g_{\mathbf{p}_t\mathbf{q}_t}\right\rangle \left\langle g_{\mathbf{p}_0\mathbf{q}_0}\middle|\phi_0^{k_0}\right\rangle e^{\omega(t)}\prod_{h=1}^{n}\frac{\tau^{k_h,k_{h-1}}}{\left|\tau^{k_h,k_{h-1}}\right|}. \end{aligned} \tag{3.4}$$

where the initial adiabat, $k_0 = k$.

## 3.2 Importance Sampling

In order to evaluate equation (3.4), we must integrate over the initial phase space $(\mathbf{p}_0,\mathbf{q}_0)$. As in section 2.2.1, this can be achieved by Monte-Carlo sampling. First, we multiply the expression through by $\frac{\langle \phi_0^k | g_{\mathbf{p}_0\mathbf{q}_0}\rangle}{\langle \phi_0^k | g_{\mathbf{p}_0\mathbf{q}_0}\rangle}$, to give

$$C_k(t) = \frac{1}{(2\pi\hbar)^N} \sum_{n=0}^{\infty} \delta_{kk_n} \int_0^t \mathrm{d}t_n \int_0^{t_n} \mathrm{d}t_{n-1} \ldots \int_0^{t_2} \mathrm{d}t_1 \int \mathrm{d}^N\mathbf{p}_0 \int \mathrm{d}^N\mathbf{q}_0 P(n)\rho(t_1, t_2 \ldots t_n)$$
$$R(\mathbf{z}_n, t) e^{\frac{iS(\mathbf{z}_n,t)}{\hbar}} \frac{\left\langle \phi_0^k | g_{\mathbf{p}_t\mathbf{q}_t}\right\rangle}{\left\langle \phi_0^k | g_{\mathbf{p}_0\mathbf{q}_0}\right\rangle} \left|\left\langle \phi_0^k | g_{\mathbf{p}_0\mathbf{q}_0}\right\rangle\right|^2 e^{\omega(t)} \prod_{h=1}^{n} \frac{\tau^{k_h,k_{h-1}}}{|\tau^{k_h,k_{h-1}}|}. \tag{3.5}$$

The integral can now be evaluated by sampling over initial coordinates $(\mathbf{p}_0, \mathbf{q}_0)$ with the probability distribution $\mathbb{P}_{\mathbf{p}_0,\mathbf{q}_0} = \left|\left\langle \phi_0^k | g_{\mathbf{p}_0\mathbf{q}_0}\right\rangle\right|^2$. We write the final expression for $C_k(t)$:

$$C_k(t) = \frac{1}{(2\pi\hbar)^N} \sum_{n=0}^{\infty} \delta_{kk_n} \int_0^t \mathrm{d}t_n \int_0^{t_n} \mathrm{d}t_{n-1} \ldots \int_0^{t_2} \mathrm{d}t_1 \int \mathrm{d}^N\mathbf{p}_0 \int \mathrm{d}^N\mathbf{q}_0 P(n)\rho(t_1, t_2 \ldots t_n)$$
$$\mathbb{P}_{\mathbf{p}_0,\mathbf{q}_0} R(\mathbf{z}_n, t) e^{\frac{iS(\mathbf{z}_n,t)}{\hbar}} \frac{\left\langle \phi_0^k | g_{\mathbf{p}_t\mathbf{q}_t}\right\rangle}{\left\langle \phi_0^k | g_{\mathbf{p}_0\mathbf{q}_0}\right\rangle} e^{\omega(t)} \prod_{h=1}^{n} \frac{\tau^{k_h,k_{h-1}}}{|\tau^{k_h,k_{h-1}}|}. \tag{3.6}$$

## 3.3 Numerical methods

In order to calculate $C_k(t)$ from equation (3.6), we must first sample trajectories starting on adiabat $k_0 = k$ with initial positions and momenta, distributed according to $\mathbb{P}_{\mathbf{p}_0,\mathbf{q}_0}$, and with initial values $S(0) = 0$, $\mathbf{M} = \mathbf{1}$ which can be determined from equations (2.1) and (2.11). We also set $\omega(0) = 0$ so that at $t = 0$, $C_k(0) = 1$. Each of these trajectories must then be classically evolved up to some final time, with a sequence of hops decided during the evolution by the instantaneous hopping probability $\lambda$ given in (2.29). To simulate this, we discretise the time into intervals, $\Delta t$. The trajectories are propagated between $t$ and $t + \Delta t$ over the current adiabat, $k$, exactly as in the single surface case. Following this, a hop to the other surface, $3 - k$, is attempted. In this section, we describe the details of implementing this numerically.

### 3.3.1 Propagation of trajectories

Between $t$ and $t+\Delta t$, each of the parameters $\mathbf{p}_t$, $\mathbf{q}_t$, $S(\mathbf{z}_n, t)$, $\mathbf{M}(t)$ are evolved classically over the current surface, exactly as in the single surface FGA method This is done according to their classical equations of motion, which for surface $k$ are given by:

$$\dot{\mathbf{p}}_t = -\frac{\partial V_k(\mathbf{q})}{\partial \mathbf{q}}, \qquad \dot{\mathbf{q}}_t = \frac{\partial T(\mathbf{p})}{\partial \mathbf{p}}, \tag{3.7}$$

$$\dot{\mathbf{S}}(t) = T(\mathbf{p}) - V_k(\mathbf{q}), \tag{3.8}$$

$$\begin{pmatrix} \dot{\mathbf{M}}_{\mathbf{pp}} & \dot{\mathbf{M}}_{\mathbf{pq}} \\ \dot{\mathbf{M}}_{\mathbf{qp}} & \dot{\mathbf{M}}_{\mathbf{qq}} \end{pmatrix} = \begin{pmatrix} -\frac{\partial^2 V(\mathbf{q})}{\partial \mathbf{q}^2}\mathbf{M}_{\mathbf{qp}} & -\frac{\partial^2 V(\mathbf{q})}{\partial \mathbf{q}^2}\mathbf{M}_{\mathbf{qq}} \\ +\frac{\partial^2 T(\mathbf{p})}{\partial \mathbf{p}^2}\mathbf{M}_{\mathbf{pp}} & +\frac{\partial^2 T(\mathbf{p})}{\partial \mathbf{p}^2}\mathbf{M}_{\mathbf{pq}} \end{pmatrix}, \tag{3.9}$$

These coupled differential equations are not analytically solvable, so must be evaluated numerically. To calculate $\mathbf{p}_t$, $\mathbf{q}_t$, $S(\mathbf{z}_n, t)$ and $\mathbf{M}(t)$, a Velocity Verlet integration scheme was chosen. This classical trajectory integrator exactly preserves the known symplectic symmetry of the monodromy matrix, decreasing the error in $R(t)$.[34] Over the time step $\Delta t$, the values are updated by evaluating the following equations:

$$\mathbf{q} \leftarrow \mathbf{q} + \frac{\Delta t}{2}\frac{\partial T(\mathbf{p})}{\partial \mathbf{p}} \tag{3.10}$$

$$S \leftarrow S + \frac{\Delta t}{2} T(\mathbf{p}) \tag{3.11}$$

$$\mathbf{M}_{\mathbf{qp}} \leftarrow \mathbf{M}_{\mathbf{qp}} + \frac{\Delta t}{2}\frac{\partial^2 T(\mathbf{p})}{\partial \mathbf{p}^2}\mathbf{M}_{\mathbf{pp}} \tag{3.12}$$

$$\mathbf{M}_{\mathbf{qq}} \leftarrow \mathbf{M}_{\mathbf{qq}} + \frac{\Delta t}{2}\frac{\partial^2 T(\mathbf{p})}{\partial \mathbf{p}^2}\mathbf{M}_{\mathbf{pq}} \tag{3.13}$$

$$\mathbf{p} \leftarrow \mathbf{p} - \Delta t\frac{\partial V_k(\mathbf{q})}{\partial \mathbf{q}} \tag{3.14}$$

$$\mathbf{q} \leftarrow \mathbf{q} + \frac{\Delta t}{2}\frac{\partial T(\mathbf{p})}{\partial \mathbf{p}} \tag{3.15}$$

$$S \leftarrow S + \frac{\Delta t}{2} T(\mathbf{p}) - \Delta t V_k(\mathbf{q}) \tag{3.16}$$

$$\mathbf{M_{pp}} \leftarrow \mathbf{M_{pp}} - \Delta t \frac{\partial^2 V_k(\mathbf{q})}{\partial \mathbf{q}^2} \mathbf{M_{qp}} \tag{3.17}$$

$$\mathbf{M_{pq}} \leftarrow \mathbf{M_{pq}} - \Delta t \frac{\partial^2 V_k(\mathbf{q})}{\partial \mathbf{q}^2} \mathbf{M_{qq}} \tag{3.18}$$

$$\mathbf{M_{qp}} \leftarrow \mathbf{M_{qp}} + \frac{\Delta t}{2} \frac{\partial^2 T(\mathbf{p})}{\partial \mathbf{p}^2} \mathbf{M_{pp}} \tag{3.19}$$

$$\mathbf{M_{qq}} \leftarrow \mathbf{M_{qq}} + \frac{\Delta t}{2} \frac{\partial^2 T(\mathbf{p})}{\partial \mathbf{p}^2} \mathbf{M_{pq}} \tag{3.20}$$

The Herman Kluk prefactor, $R(\mathbf{z}_n, t)$ can be calculated during simulation from the elements of the monodromy matrix using equation (2.10), and has the form $R(\mathbf{z}_n, t) = \sqrt{c}$, where $c$ is in general a complex number given by $c = \det\left(\frac{1}{2}(\mathbf{M_{pp}} + \mathbf{M_{qq}} - i\mathbf{M_{qp}} + i\mathbf{M_{pq}})\right)$. The square root of a complex number is not uniquely defined, and there will exist a branch cut in the value of $R(\mathbf{z}_n, t)$ as the argument of $c$ crosses the negative real axis. As $R(\mathbf{z}_n, t)$ is defined as being continuous with time[37], in simulation the value of $R(\mathbf{z}_n, t)$ is multiplied by a phase factor, $I = e^{\nu\pi i}$, where $\nu$ is the Maslov index, which is equal to the number of times that the argument of $c$ has crossed the negative real axis during evolution.

The value $\omega(t)$ is also required to evaluate equation (3.6), and can be calculated by numerical integration of its derivative,

$$\dot{\omega} = |\tau(t)|, \tag{3.21}$$

where $\tau(t)$ is given in equation (2.32). In this implementation, the trapezium rule was found to be a sufficient.

### 3.3.2 Force and Hessian evaluations

For a trajectory evolving on surface $k$, in order to evaluate equations (3.10)-(3.20) we require the potential energy $V_k$, the forces $\frac{\partial V_k(\mathbf{x})}{\partial \mathbf{x}}$, and Hessian matrix $\frac{\partial^2 V_k(\mathbf{x})}{\partial \mathbf{x}^2}$. In addition, the derivative coupling element $\mathbf{d}_{3-k,k}$ is required to evaluate $\tau(t)$ in (2.32).

In order to determine these quantities for a trajectory at position **x**, we first evaluate $\mathbf{U}(\mathbf{x})$, which is the $2\times 2$ matrix for the potential energy of the system in the diabatic basis, where the nuclear kinetic energy $\hat{T}_n$ is diagonal. This is the form in which the models for pyrazine that we will be considering are parametrised, with the energy of the $j^{th}$ diabat at **x** given by the element $U_{jj}(\mathbf{x})$, and the coupling between the diabats described by the off-diagonal elements.

To find the adiabatic potentials $V_1$ and $V_2$ at position **x**, we use a similarity transform to diagonalise $U(\mathbf{x})$, which gives

$$\Omega(\mathbf{x})\mathbf{U}(\mathbf{x})\Omega^{-1}(\mathbf{x}) = \Omega(\mathbf{x})\begin{pmatrix} U_{11}(\mathbf{x}) & U_{12}(\mathbf{x}) \\ U_{21}(\mathbf{x}) & U_{22}(\mathbf{x}) \end{pmatrix}\Omega^{-1}(\mathbf{x}) = \begin{pmatrix} V_1(\mathbf{x}) & 0 \\ 0 & V_2(\mathbf{x}), \end{pmatrix} \tag{3.22}$$

where $\Omega(\mathbf{x})$ has the form of a rotation matrix:

$$\Omega(\mathbf{x}) = \begin{pmatrix} \cos(\theta(\mathbf{x})) & -\sin(\theta(\mathbf{x})) \\ \sin(\theta(\mathbf{x})) & \cos(\theta(\mathbf{x})) \end{pmatrix}. \tag{3.23}$$

$\theta(\mathbf{x})$ is the diabatic-adiabatic rotation angle at position **x**, and can be written in terms of $\mathbf{U}(\mathbf{x})$ as:

$$\theta(\mathbf{x}) = \frac{1}{2}\arctan\left(\frac{2U_{12}(\mathbf{x})}{U_{11}(\mathbf{x}) - U_{22}(\mathbf{x})}\right) \tag{3.24}$$

The potentials $V_1$ and $V_2$ can also be found in terms of $\mathbf{U}(\mathbf{x})$, and are given by:

$$V_1(\mathbf{x}) = \frac{U_{11}(\mathbf{x}) + U_{22}(\mathbf{x})}{2} - \frac{1}{2}\left(\left(U_{11}(\mathbf{x}) - U_{22}(\mathbf{x})\right)^2 + 4U_{12}^2(\mathbf{x})\right)^{\frac{1}{2}}, \tag{3.25}$$

$$V_2(\mathbf{x}) = \frac{U_{11}(\mathbf{x}) + U_{22}(\mathbf{x})}{2} + \frac{1}{2}\left(\left(U_{11}(\mathbf{x}) - U_{22}(\mathbf{x})\right)^2 + 4U_{12}^2(\mathbf{x})\right)^{\frac{1}{2}}. \tag{3.26}$$

In order to find the Hessian and derivative coupling, we consider the Schrödinger equation in the adiabatic representation:

$$\hat{H}_e(\mathbf{x})|\chi_k(\mathbf{x})\rangle\!\rangle = V_k(\mathbf{x})|\chi_k(\mathbf{x})\rangle\!\rangle, \tag{3.27}$$

where $\hat{H}_e(\mathbf{x}) = \Omega(\mathbf{x})U(\mathbf{x})\Omega^{-1}(\mathbf{x})$ and the use of double angle brackets denotes an inner product,

$$\langle\!\langle\chi_j(\mathbf{x})|\chi_k(\mathbf{x})\rangle\!\rangle = \int \mathbf{dr}\chi_j^*(\mathbf{r};\mathbf{x})\chi_k^*(\mathbf{r};\mathbf{x}). \tag{3.28}$$

Differentiating equation (3.27) once with respect to the normal mode coordinate $\mathrm{x}_j$, followed by premultiplication by the orthonormal state $\langle\!\langle\chi_l(\mathbf{x})|$ gives

$$\langle\!\langle\chi_l(\mathbf{x})|\frac{\partial\hat{H}_e(\mathbf{x})}{\partial\mathrm{x}_j}|\chi_k(\mathbf{x})\rangle\!\rangle + \langle\!\langle\chi_l(\mathbf{x})|\hat{H}_e(\mathbf{x})|\frac{\partial\chi_k(\mathbf{x})}{\partial\mathrm{x}_j}\rangle\!\rangle = \frac{\partial V_k(\mathbf{x})}{\partial\mathrm{x}_j}\delta_{lk} + V_k(\mathbf{x})\langle\!\langle\chi_l(\mathbf{x})|\frac{\partial\chi_k(\mathbf{x})}{\partial\mathrm{x}_j}\rangle\!\rangle. \tag{3.29}$$

Due to the Hermiticity of $\hat{H}_e(\mathbf{x})$, $\langle\!\langle\chi_l(\mathbf{x})|\hat{H}_e(\mathbf{x}) = \langle\!\langle\chi_l(\mathbf{x})|V_l(\mathbf{x})$. From (2.23), the term $\langle\!\langle\chi_l(\mathbf{x})|\frac{\partial\chi_k(\mathbf{x})}{\partial\mathrm{x}_j}\rangle\!\rangle$ can be recognised as an element of the derivative coupling matrix, $(d_{lk})_j$, so the equation becomes:

$$\langle\!\langle\chi_k(\mathbf{x})|\frac{\partial\hat{H}_e(\mathbf{x})}{\partial\mathrm{x}_j}|\chi_l(\mathbf{x})\rangle\!\rangle = \frac{\partial V_l(\mathbf{x})}{\partial\mathrm{x}_j}\delta_{lk} + (V_l(\mathbf{x}) - V_k(\mathbf{x}))(d_{lk})_j \tag{3.30}$$

For the case where $l = k$, $(d_{ll})_j = (d_{kk})_j = 0$ (which is proved in Appendix A). Using this, we get an expression for $\frac{\partial V_k(\mathbf{x})}{\partial\mathrm{x}_j}$:

$$\frac{\partial V_k(\mathbf{x})}{\partial\mathrm{x}_j} = \langle\!\langle\chi_k(\mathbf{x})|\frac{\partial\hat{H}_e(\mathbf{x})}{\partial\mathrm{x}_j}|\chi_k(\mathbf{x})\rangle\!\rangle. \tag{3.31}$$

If, instead, we set $l \neq k$ in equation (3.30) we arrive at an expression for the derivative coupling between surfaces $k$ and $l$,

$$(d_{lk})_j = \frac{\langle\!\langle\chi_l(\mathbf{x})|\frac{\partial\hat{H}_e(\mathbf{x})}{\partial\mathrm{x}_j}|\chi_k(\mathbf{x})\rangle\!\rangle}{(V_k(\mathbf{x}) - V_l(\mathbf{x}))}. \tag{3.32}$$

An expression for the Hessian matrix can be found by differentiating (3.27) twice with respect to **x** followed by premultiplication by $\langle\!\langle\chi_l(\mathbf{x})|$ to give:

$$\begin{aligned}\langle\!\langle\chi_l(\mathbf{x})|\frac{\partial^2\hat{H}_e(\mathbf{x})}{\partial\mathrm{x}_j\partial\mathrm{x}_i}|\chi_k(\mathbf{x})\rangle\!\rangle+\langle\!\langle\chi_l(\mathbf{x})|\frac{\partial\hat{H}_e(\mathbf{x})}{\partial\mathrm{x}_i}|\frac{\partial\chi_k(\mathbf{x})}{\partial\mathrm{x}_j}\rangle\!\rangle+\langle\!\langle\chi_l(\mathbf{x})|\frac{\partial\hat{H}_e(\mathbf{x})}{\partial\mathrm{x}_j}|\frac{\partial\chi_k(\mathbf{x})}{\partial\mathrm{x}_i}\rangle\!\rangle \\ =(d_{lk})_j\left(\frac{\partial V_k}{\partial\mathrm{x}_i}+\frac{\partial V_k}{\partial\mathrm{x}_j}\right)+\frac{\partial^2 V_k}{\partial\mathrm{x}_j\partial\mathrm{x}_i}\delta_{lk}+(V_k-V_l)\langle\!\langle\chi_l(\mathbf{x})|\frac{\partial^2\chi_k(\mathbf{x})}{\partial\mathrm{x}_j\partial\mathrm{x}_i}\rangle\!\rangle,\end{aligned}\tag{3.33}$$

which for $l=k$ reduces to

$$\frac{\partial^2 V_k}{\partial\mathrm{x}_j\partial\mathrm{x}_i}=\langle\!\langle\chi_k(\mathbf{x})|\frac{\partial^2\hat{H}_e(\mathbf{x})}{\partial\mathrm{x}_j\partial\mathrm{x}_i}|\chi_k(\mathbf{x})\rangle\!\rangle+\langle\!\langle\chi_k(\mathbf{x})|\frac{\partial\hat{H}_e(\mathbf{x})}{\partial\mathrm{x}_i}|\frac{\partial\chi_k(\mathbf{x})}{\partial\mathrm{x}_j}\rangle\!\rangle+\langle\!\langle\chi_k(\mathbf{x})|\frac{\partial\hat{H}_e(\mathbf{x})}{\partial\mathrm{x}_j}|\frac{\partial\chi_k(\mathbf{x})}{\partial\mathrm{x}_i}\rangle\!\rangle.\tag{3.34}$$

The last two terms appearing in (3.34) can be evaluated by inserting the identity operator:

$$\hat{\mathbf{1}}=\sum_{l=1}^{2}|\chi_l(\mathbf{x})\rangle\!\rangle\langle\!\langle\chi_l(\mathbf{x})|,\tag{3.35}$$

which gives

$$\begin{aligned}\frac{\partial^2 V_k}{\partial\mathrm{x}_j\partial\mathrm{x}_i}=&\langle\!\langle\chi_k(\mathbf{x})|\frac{\partial^2\hat{H}_e(\mathbf{x})}{\partial\mathrm{x}_j\partial\mathrm{x}_i}|\chi_k(\mathbf{x})\rangle\!\rangle+\sum_{l=1}^{2}\langle\!\langle\chi_k(\mathbf{x})|\frac{\partial\hat{H}_e(\mathbf{x})}{\partial\mathrm{x}_i}|\chi_l(\mathbf{x})\rangle\!\rangle\langle\!\langle\chi_l(\mathbf{x})||\frac{\partial\chi_k(\mathbf{x})}{\partial\mathrm{x}_j}\rangle\!\rangle \\ &+\sum_{l=1}^{2}\langle\!\langle\chi_k(\mathbf{x})|\frac{\partial\hat{H}_e(\mathbf{x})}{\partial\mathrm{x}_j}|\chi_l(\mathbf{x})\rangle\!\rangle\langle\!\langle\chi_l(\mathbf{x})|\frac{\partial\chi_k(\mathbf{x})}{\partial\mathrm{x}_i}\rangle\!\rangle.\end{aligned}\tag{3.36}$$

Using equation (2.23), the expression for the Hessian matrix can also be written in terms of the derivative coupling matrix as

$$\frac{\partial^2 V_k}{\partial\mathrm{x}_j\partial\mathrm{x}_i}=\langle\!\langle\chi_k(\mathbf{x})|\frac{\partial^2\hat{H}_e(\mathbf{x})}{\partial\mathrm{x}_j\partial\mathrm{x}_i}|\chi_k(\mathbf{x})\rangle\!\rangle+\big(V_l(\mathbf{x})-V_k(\mathbf{x})\big)\sum_{l=1}^{2}\big(|(d_{lk})_i|^2+|(d_{lk})_j|^2\big).\tag{3.37}$$

### 3.3.3 Stochastic Surface Hopping

After classical evolution over a time $\Delta t$, a hop from the current surface $k$ to the other surface $3-k$ is attempted based on the hopping rate,

$$\lambda=\left|\tau^{3-k,k}\right|\Delta t.\tag{3.38}$$

This will correctly sample the integral over the inhomogeneous Poisson distribution $P(n)\rho(t_1, t_2 \ldots t_n)$ in the limit that $\Delta t \rightarrow 0$. This means that computationally, $\Delta t$, must be small enough that the probability of hopping twice within a time period of $\Delta t$ is negligible.[36]

## Chapter 4

# The 4-mode Pyrazine model

In this chapter, the FGA-SH theory developed in Chapters 2 and 3 will be used to simulate the gas phase absorption spectrum of pyrazine. To treat the 24 vibrational modes of pyrazine using the Time Dependent Schrödinger equation, a Hamiltonian would have to be constructed in a basis which, for an accurate description of the molecule, would include at least 10 states for each vibrational mode. This would yield a Hilbert space with a size of approximately ~ $10^{24}$. This is an unfeasibly large matrix and it is unlikely that it would ever be possible to store it in memory, let alone diagonalise it.

We first consider the four mode model proposed by Woywod et al.[24], which has a corresponding Hilbert space of ~ $10^5$ states. This is small enough that the Schrödinger equation can be solved to determine the eigenvalues and eigenvectors required to construct the absorption spectrum using Equation (1.1). The quantum simulations with Woywod's set of parameters provide clean spectra, free of experimental noise with which to make a direct comparison to those performed using the FGA-SH method. This is particularly important as the experimental data, shown in 1.4, was obtained at room temperature, whereas in this thesis the system is considered to be at 0 Kelvin before photoexcitation[24]. Therefore, not all the spectral features seen in experiment are expected to be reproducible through simulation. Despite the model lacking twenty of the vibrational normal modes, it will be shown by symmetry arguments that the remaining four overwhelmingly determine the shape of both $S_1$ and $S_2$ regions.

## 4.1 Model Hamiltonian

The four vibrational modes that Woywod chose to retain in his model are presented in table 4.1

| | Mode | Symmetry |
|---|---|---|
| 1 | $\nu_{10a}$ | $\Gamma_{B_{1g}}$ |
| 2 | $\nu_1$ | $\Gamma_{A_g}$ |
| 3 | $\nu_{6a}$ | $\Gamma_{A_g}$ |
| 4 | $\nu_{9a}$ | $\Gamma_{A_g}$ |

**Table 4.1** The vibrational normal modes and their symmetries retained in the 4 dimensional model for pyrazine.

The model Hamiltonian, expressed in the diabatic basis, in which $|1\rangle = S_1$ and $|2\rangle = S_2$, can written as

$$\mathcal{H} = \begin{pmatrix} \mathcal{H}_1 & \lambda \mathrm{q}_{10a} \\ \lambda \mathrm{q}_{10a} & \mathcal{H}_2 \end{pmatrix}. \tag{4.1}$$

The diagonal $\mathcal{H}_k$ terms describe the energy of the $k^{th}$ diabat, $S_k$:

$$\mathcal{H}_1 = E_1 + \mathcal{H}_0 + \boldsymbol{\kappa}^{(1)} \cdot \mathbf{q} + \mathbf{q}^{\top} \boldsymbol{\gamma}^{(1)} \mathbf{q}, \tag{4.2}$$

$$\mathcal{H}_2 = E_2 + \mathcal{H}_0 + \boldsymbol{\kappa}^{(2)} \cdot \mathbf{q} + \mathbf{q}^{\top} \boldsymbol{\gamma}^{(2)} \mathbf{q}. \tag{4.3}$$

Here, $E_k$ is the vertical excitation energy from the ground state to $S_k$, and $\mathcal{H}_0$ is the Hamiltonian for the ground state, $S_0$, which is approximated as an 4 dimensional harmonic oscillator with frequencies $\omega_i$:

$$\mathcal{H}_0 = \sum_i^4 \frac{\omega_i}{2} \left( - \frac{\partial^2}{\partial q_i^2} + q_i^2 \right) \tag{4.4}$$

The last two terms in 4.2 correct for differences in the geometry of the excited states relative to $S_0$. The term $\boldsymbol{\kappa}^{(k)} \mathbf{q}$ describes the amount by which the excited state is shifted from the ground state equilibrium geometry, centred at $\mathbf{q} = 0$. The quadratic term $\mathbf{q}^\top\boldsymbol{\gamma}^{(k)}\mathbf{q}$ accounts for changes in the frequencies of the normal modes on going from $S_0$ to $S_k$.

In this model, the coupling between the $S_1$ and $S_2$ surfaces comes from only one term, which is the linear function, $\lambda\mathbf{q}$, appearing on the off-diagonals in (4.1) . To see why only this term is retained, we note that it is necessary that it transforms as the totally symmetric representation, $\Gamma_{A_g}$. Therefore,

$$\Gamma_{A_g} = \Gamma_{S_1} \otimes \Gamma_{\mathbf{q}} \otimes \Gamma_{S_2} = \Gamma_{B_{3u}} \otimes \Gamma_{\mathbf{q}} \otimes \Gamma_{B_{2u}} = \Gamma_{B_{1u}} \otimes \Gamma_{\mathbf{q}}. \tag{4.5}$$

which, as $D_{2h}$ is an Abelian point-group so that each element is its own unique inverse, gives that $\Gamma_{\mathbf{q}} = \Gamma_{B_{1u}}$. Examining the symmetries of all 24 modes, which are given in equation (1.16), we see that there is only one with this symmetry, $\nu_{10a}$, which explains why this mode must be retained in the model.

As the system is taken to be at $0K$ before photoexcitation, it will start in the lowest vibrational level of the ground state, which for pyrazine, a closed-shell system, means that $\Gamma_0 = \Gamma_{A_g}$. Since the transition dipole moments to the $S_1$ and $S_2$ electronic states have the same symmetries as these electronic states ($B_{3u}$ and $B_{2u}$, respectively), it follows that only $A_g$ vibrational normal modes will be Franck-Condon active, and it is these alone that contribute to the frequencies of the peaks in the spectrum. Woywod et al. retained the $\nu_1$, $\nu_{6a}$ and $\nu_{9a}$ modes in their Hamiltonian as, of the totally symmetric modes, these have the largest values of $\kappa$, which controls the change in the equilibrium geometry on excitation and therefore the relative Franck-Condon activity.

The parameters used in the simulations are taken from ab-initio complete-active-space self-consistent field (CASSCF) and multireference configuration interaction (MRCI) calculations performed by Woywod et al.[24]. They are shown in tables 4.2 and 4.3. Woywood chose to neglect all quadratic coupling constants except $\gamma^{(1,2)}_{q_{10a}q_{10a}}$, which has a significantly larger magnitude than the others. Note that the gradient $\kappa^{(1,2)}$ is exactly zero by symmetry for the $B_{1g}$ symmetry $\nu_{10a}$ mode.

| Mode | $\omega$ ($cm^{-1}$) | $\kappa^{(1)}$ (eV) | $\kappa^{(2)}$ (eV) |
|---|---|---|---|
| $\nu_{10a}$ | 919.0 | 0.0000 | 0.0000 |
| $\nu_1$ | 1015.0 | −0.0470 | −0.2012 |
| $\nu_{6a}$ | 596.0 | −0.0964 | 0.1193 |
| $\nu_{9a}$ | 1230.0 | 0.1594 | 0.0484 |

**Table 4.2** The vibrational frequencies and linear on-diagonal coefficients for the 4 mode model

| $E_1(eV)$ | $E_2(eV)$ | $\lambda$(eV) | $\gamma^{(1,2)}_{q_{10a}q_{10a}}$ (eV) |
|---|---|---|---|
| 4.0119 | 4.9619 | 0.1825 | −0.0180 |

**Table 4.3** The excitation energies and coupling terms for the 4 mode model

## 4.2 Matrix representation

In order to evaluate the absorption spectrum quantum mechanically, we must specify the wavefunction in a basis set of all the available vibronic states.

$$|\Psi_{j,v}\rangle = |\Psi_j\rangle \otimes |\Psi_v\rangle \tag{4.6}$$

where $|\Psi_j\rangle$ is the $S_j$ electronic state, and $|\Psi_v\rangle$ is the vibrational state, which can be expanded as a direct product of the four normal modes:

$$|\Psi_v\rangle = |\nu_{10a}\rangle \otimes |\nu_1\rangle \otimes |\nu_{6a}\rangle \otimes |\nu_{9a}\rangle . \tag{4.7}$$

Each of these four states is represented by a basis set of vibrational energy levels $|\nu_i\rangle = 0, 1, 2, 3\ldots$ and is truncated at a maximum level for each mode. The number of such levels is given in table 4.4.

The symmetry of the total wavefunction, $|\Psi_{j,v}\rangle$, is dictated by the electronic state, $|\Psi_j\rangle$ and the only non-symmetric mode, $\nu_{10a}$. If $|\nu_{10a}\rangle$ is even, its symmetry is $\Gamma_{A_g}$ so the wavefunction will have the symmetry of $|\Psi_j\rangle$ which is $B_{3u}$ for $S_1$ or $B_{2u}$ for $S_2$. If $|\nu_{10a}\rangle$ is odd, it has $B_{1g}$ symmetry so the wavefunction transforms as $\Gamma_j \otimes \Gamma_{B_{1g}}$, which

| Mode | Number of States |
|---|---|
| $\nu_{10a}$ | 22 |
| $\nu_1$ | 18 |
| $\nu_{6a}$ | 18 |
| $\nu_{9a}$ | 12 |

**Table 4.4** The number of vibrational states retained for each mode

again is one of $B_{3u}$ or $B_{2u}$. Since each Hamiltonian matrix element must necessarily transform as $\Gamma_{A_g}$, the Hamiltonian will contain two blocks: one that connects the $B_{3u}$ states and the other connecting $B_{2u}$ states. These blocks can be diagonalised separately, each spanning half of the total Hilbert space which has a basis set of $22 \times 18 \times 18 \times 12 = 85,536$.

Following the convention of Woywod, we will refer to the eigenvalues generated by diagonalising $B_{3u}$ and $B_{2u}$ blocks as the $S_1$ and $S_2$ spectra respectively.[24] Although each spectrum contributes predominately to its eponymous region, the resulting eigenvalues do overlap, with some peaks in the $S_1$ spectrum featuring in the $S_2$ region and vice versa.

## 4.3 Quantum Simulations

The eigenvectors and eigenvalues were found by diagonalising the matrix Hamiltonian using the efficient method outlined by Ian Craig[38],which starts by rendering the matrix tridiagonal, by use of the Lanczos algorithm. This algorithm exploits the fact that the $n \times n$ Hamiltonian, where for this problem $n = 85,536$, is sparse, with only $\mathcal{O}(n)$ non-zero elements, to accomplish the tridiagonalisation with a relatively small number of matrix-vector multiplications. After being rendered tridiagonal, the matrix can be quickly diagonalised to give the values of $E_k$ and $|k\rangle$.

In order to compare to experiment, both $S_1$ and $S_2$ simulated spectra must be combined. To do this, we used the fact that promotion to the $S_2$ level, which is a $\pi \rightarrow \pi^*$ transition, has an oscillator strength 10.0 times as large as the $n \rightarrow \pi^*$ transition for $S_1$.[39] Thus the spectrum in the $S_2$ range is entirely dominated by just the $S_2$ spectrum. On the other hand both spectra need to be weighted and combined in the $S_1$ range.

Although the 20 modes neglected in this model do not contribute to the frequencies, they do have an effect on the widths and intensities of the peaks. In general, they couple to the active modes and dissipate their energy (a process called intrastate vibrational relaxation)[24], which leads to a shorter decay time $\tau$, and thus a larger uncertainty in the energy (since $\Delta E \Delta \tau \geq \frac{\hbar}{2}$). To account for this, Woywod et al. convoluted the stick spectrum generated by quantum simulation, $P(E)$, with a Lorentzian to give $\tilde{P}(E)$, where, for spectrum $S_j$,

$$\tilde{P}_j(E) = \frac{1}{\pi T_{2_j}} \sum_k \frac{|\langle \Psi_0 | k \rangle| t^2}{(E - E_k)^2 + (\frac{1}{T_{2_j}})}, \tag{4.8}$$

where $T_{2_j}$ is a phenomenological constant chosen to produce the same linewidths for the $S_j$ spectrum as are seen in experiment. For $S_1$, $T_{2_1} = 500$fs and for $S_2$, $T_{2_2} = 30$fs.

The quantum simulations were performed by Joseph Lawrence and the resulting absorption spectra in the $S_1$ and $S_2$ ranges are shown in Figures 4.1 and 4.3 respectively, alongside the experimental results. In Figure 4.2, we have also depicted the components of the $S_1$ and $S_2$ spectra that are in the $S_1$ region which are combined to obtain Figure 4.3.

From Figure 4.1, we observe that there is a qualitative agreement between the spectra in the $S_1$ region, with the three highest peaks clearly reproduced. However, there is quite poor agreement between the spectra at lower wavelengths, with the experimental spectrum exhibiting many more peaks with lower intensities than in simulation. The cause of the difference has been attributed to strong Fermi resonance interaction between the $\nu_{6a}$, $\nu_{9a}$ and $\nu_{10a}$ modes. It appears that in general, the model underestimates the degree of coupling. This discrepancy is in part due to the fact that the experimental data was obtained at room temperature, so hot bands

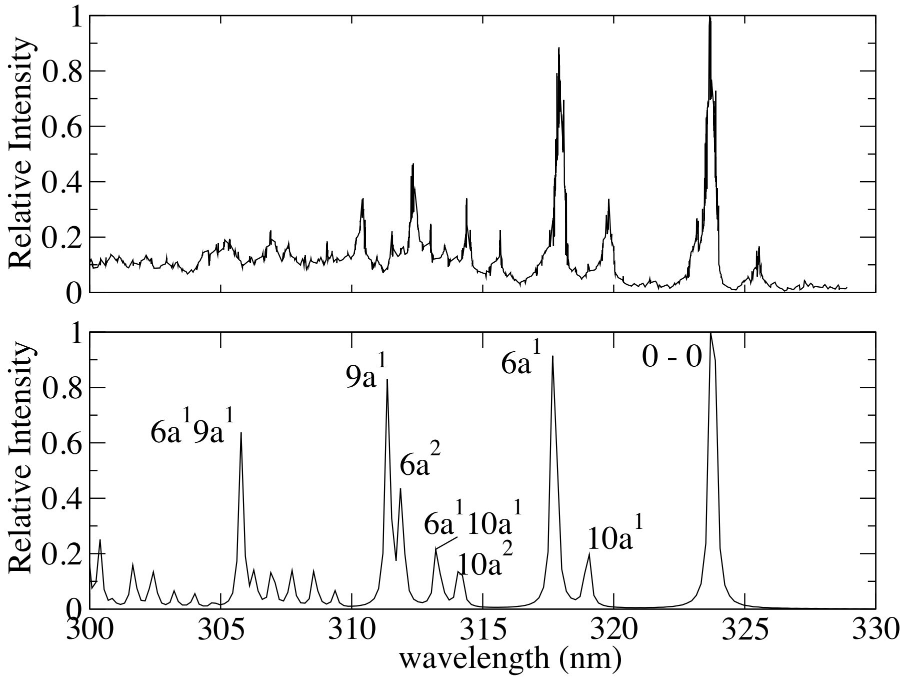

**Figure 4.1** Upper panel: Experimental result in the $S_1$ region, lower panel: quantum simulation of the $S_1$ absorption spectrum. Simulation performed by Joseph Lawrence.

are present which will not appear in the 0 K model. Most notably, the peak at 326 nm, which is at a higher wavelength than the 0 – 0 peak must be a hot band, and has been attributed to the $v_{16b}^1 \rightarrow v'^1_{16b}$ transition.[40]

In the case of the $S_2$ spectrum, shown in Figure 1.4, we observe a highly satisfactory agreement between the shape of the spectrum predicted by the 4 mode model and experiment, showing that the coupling between surfaces is accurately captured in Woywod's model. It was found that in simulation, the spectrum was shifted 3.7 nm lower in wavelength than experiment. This originates from error in the vertical excitation energy term $E_2$. Following Woywod[24], in presenting the spectrum we have corrected for this in order to facilitate comparison between the vibronic excitation peaks.

It is clear that in order to evaluate the effectiveness of the semiclassical theory we should compare our results to the quantum simulations so as to eliminate the considerable systematic discrepancy in the model's parameterisation. In this thesis, we concentrate on simulating the $S_1$ spectrum, which appears in the upper panel of

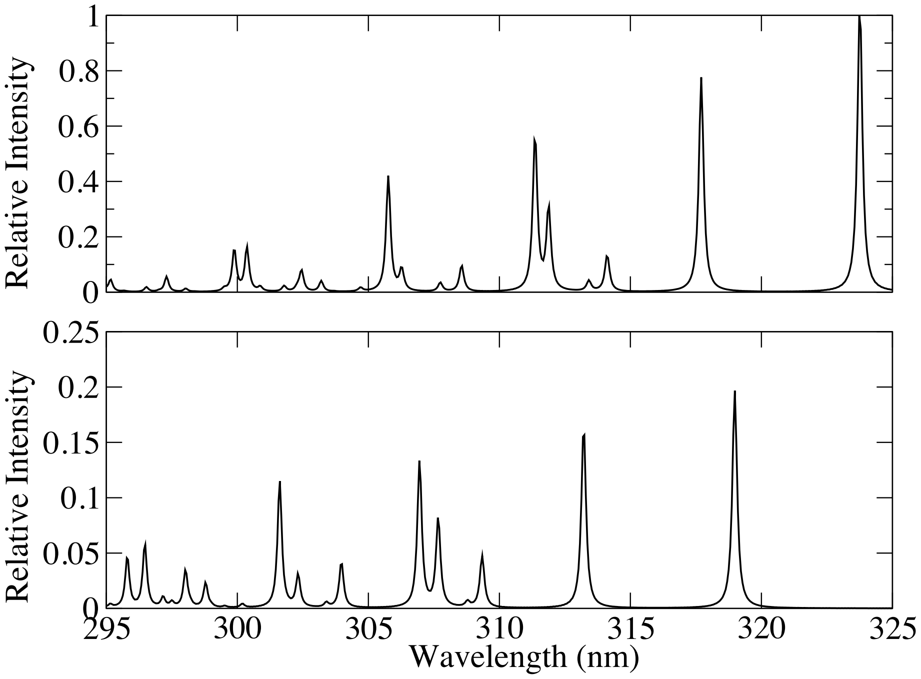

**Figure 4.2** Quantum simulations for the $S_1$ region. Upper panel: the contribution from the $S_1$ spectrum, lower panel: the contribution from the $S_2$ spectrum. Simulation performed by Joseph Lawrence.

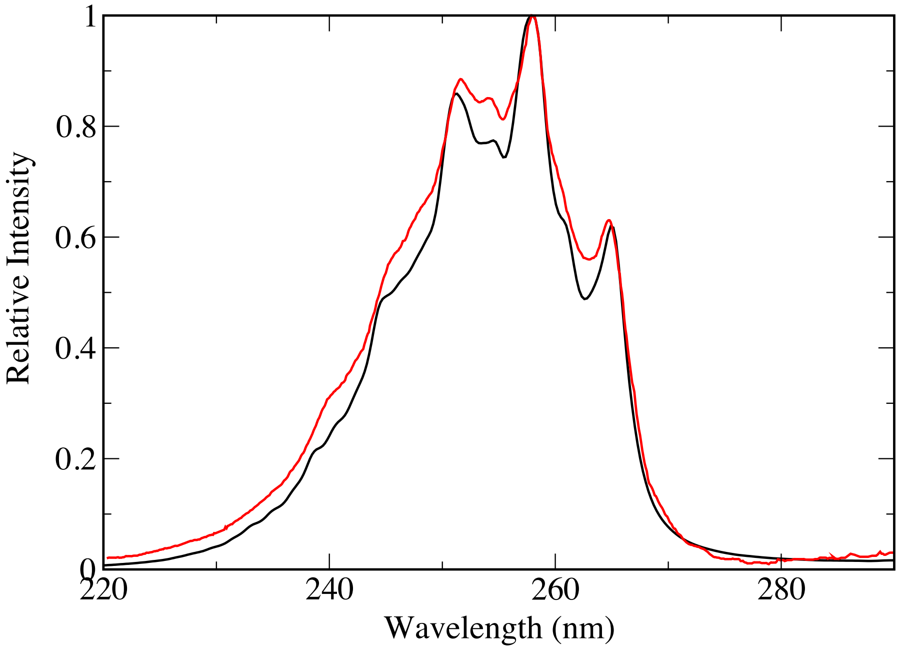

**Figure 4.3** Quantum simulation of the $S_2$ absorption spectrum (black) compared to the experimental result[26] (red). Simulation performed by Joseph Lawrence.

Figure 4.2 and the $S_2$ spectrum in Figure 4.3.

## 4.4 FGA-SH Simulations: The need for an algorithm

A first attempt to simulate the spectra using the FGA-SH method was made, implementing the numerical methods outlined in Chapter 3. It was found, however, that for both $S_1$ and $S_2$ spectra it was not possible to converge the autocorrelation function over even a short ($< 100\,\mathrm{fs}$) window of time. The reason for this can be attributed to an exponential growth in the terms $R(\mathbf{z}_n, t)$ and $e^{\omega(t)}$ that appear in equation (3.6). This is a problem that is commonly encountered when evaluating autocorrelation functions using trajectory methods with phase information[41].

The growth in $R(\mathbf{z}_n, t)$ is a result of the elements of the monodromy matrix growing with time proportional to $e^{\lambda t}$, where $\lambda$ is the Lyapunov number for an initial point in phase space.[42] When $\lambda > 0$, this leads to exponential growth of $R(\mathbf{z}_n, t)$ for some of the trajectories, and therefore requires an exponentially greater number of them to be averaged over in order to converge C(t), whose magnitude has to be less than one at all times.

The factor $e^{\omega(t)}$, present in equation (3.6), was found to increase the variance in addition to the Herman Kluk prefactor. Since $\omega(t)$ is the integral over $|\mathbf{p}(t) \cdot \mathbf{d}_{k\prime,k}|$ from 0 to $t$, it is positive for all time and thus contributes a similar exponential scaling to that observed with $R(\mathbf{z}_n, t)$. This growth will become particularly large for trajectories that pass close to the conical intersection, as in that region the expression for $\mathbf{d}_{k\prime,k}$, given in (3.32), tends towards infinity. This means that the integral may be rendered impossible to converge by just one trajectory passing through the conical intersection.

It is therefore critical that an algorithm is employed that deals with such trajectories. Two approaches are considered in this thesis: a birth-death branching algorithm suggested by Lu and Zhou[18] and an algorithm for progressively damping the contributions of trajectories with large prefactors, motivated by Filinov smoothing[41].

### 4.4.1 Branching Algorithm

The birth-death branching algorithm works by periodically splitting trajectories into a number of smaller ones according to their weight, $|\Gamma(t)|$, where $\Gamma(t) = R(\mathbf{z}_n, t)e^{\omega(t)}$. These split trajectories are initially identical to the parent but due to the stochastic nature of the surface hopping, they take divergent paths. This allows the phase space associated with chaotic trajectories to be better explored, giving a more accurate contribution to the integral and thus reducing the variance in $C(t)$.

To employ the algorithm, every $N_{branch}$ steps a random number $\xi$, which is uniformly distributed on $[0,1]$, is generated for each trajectory. Then, taking $[|\Gamma(t)|]$ to be the integer part of $|\Gamma(t)|$, each trajectory is branched according to the following criteria:

- If $\xi \leq |\Gamma(t)| - [|\Gamma(t)|]$ then replace the trajectory with $[|\Gamma(t)|] + 1$ trajectories that are identical to the parent except that their weights $\gamma(t) = \frac{\Gamma(t)}{|\Gamma(t)|}$.

- If $\xi > |\Gamma(t)| - [|\Gamma(t)|]$ then replace the trajectory with $[|\Gamma(t)|]$ trajectories that are identical to the parent except that their weights $\gamma(t) = \frac{\Gamma(t)}{|\Gamma(t)|}$. If $[|\Gamma(t)|] = 0$ then this trajectory is killed and does not contribute to the integral at later times.

On average this process will conserve the total weight $\sum_{\alpha}^{M(t)} \Gamma(t)$, where $M(t)$ is the number of trajectories at time $t$, but will redistribute it between $\sim \sum_{\alpha}^{M(t)} \Gamma(t)$ trajectories with weights $|\gamma(t)| \sim 1$. The sum over these trajectories will converge more rapidly as they are effectively bound to a unit circle on the complex plane.

### 4.4.2 Prefactor Damping Algorithm

A different method for dealing with the chaotic trajectories is to suppress the weights with which they contribute to the integral in equation (3.6). A primitive method for doing this in the single surface case was suggested by Kay[42], where trajectories whose prefactors, $|R(t)|$, grew larger than some maximum value, $R_{(max)}$, were simply removed from the simulation at later times. The rationale for this is that these trajectories are chaotic in the sense that a small change in their initial coordinates $(\mathbf{p}_i,\mathbf{q}_i)$ will lead to a large change in their final values, including the phase of $R(t)$. Therefore they will largely cancel each other out, so their net contribution to the integral will be small.

It can be seen that the difficulty in converging the integral in equation (3.6) using Monte-Carlo trajectories stems from the oscillatory nature of the integrand. Filinov smoothing is an analytical method for reducing the oscillatory character of the integrand, which, in the single surface case, gives a new expression for $R(t)$ by replacing the terms appearing in equation (3.6) by truncated Taylor expansions around the initial coordinates $(\mathbf{p}_i,\mathbf{q}_i)$.[43] This introduces an additional oscillatory component into the integral which works to smooth it, leading to faster convergence.[44] Two parameters, $\alpha$ and $\beta$, control the smoothness of the integrand. For small $\alpha$ and $\beta$, the expression is a poor approximation, but in the limit that $\alpha,\beta \to \infty$ the original FGA result is recovered.[41] In the Filinov smoothed expression, $R(t)$ becomes $\Gamma_{\alpha,\beta}$, which for small values of $R(t)$ is identical, but as $R(t)$ increases, the magnitude of $\Gamma_{\alpha,\beta}$ is damped, and tends towards 0.

The Filinov smoothing method is less ad-hoc than Kay's and has been shown to be much more efficient.[41] However, it is not possible to use an analytical smoothing method for FGA-SH as the hopping sequence means that $R(\mathbf{z}_n,t)$ evolves stochastically. Furthermore, we must also consider the exponential growth of the $e^{\omega(t)}$ term. We chose to employ a method for damping the combined weight $\Gamma(t) = R(\mathbf{z}_n,t)e^{\omega(t)}$ on the fly, in the the same spirit as Filinov's method. This 'prefactor damping' tech-

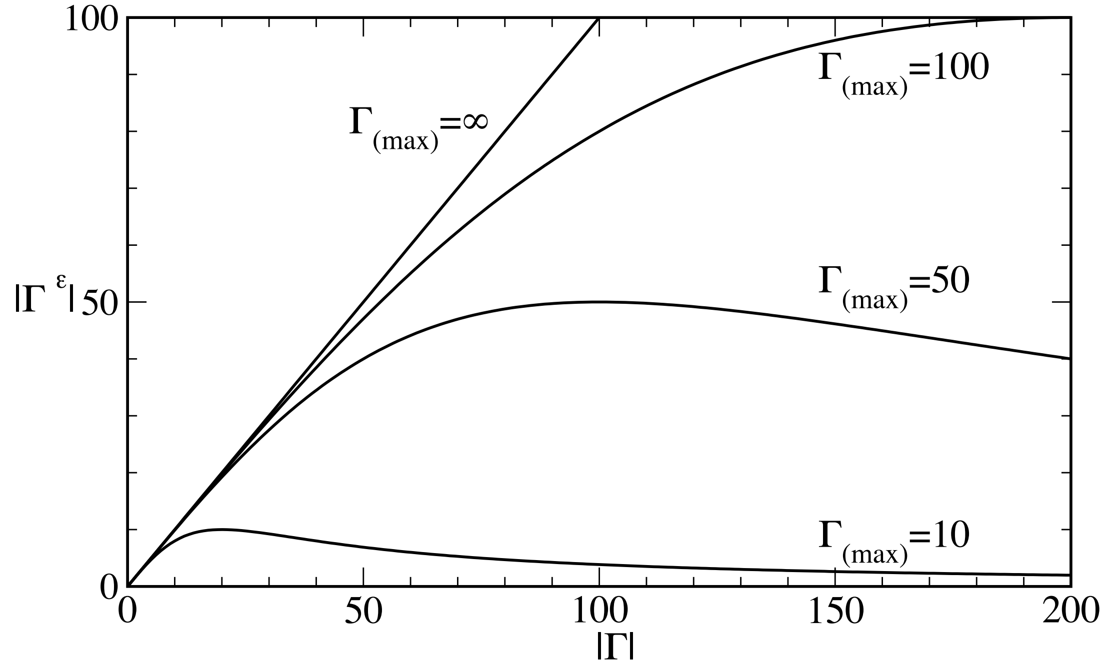

**Figure 4.4** Plot of $\left|\Gamma^{(\epsilon)}\right|$ against $|\Gamma|$ for different values of $\Gamma_{(max)}$.

nique works by replacing the calculated value of $\Gamma(t)$ with $\Gamma^{(\epsilon)}(t)$, where

$$\Gamma^{(\epsilon)}(t) = \frac{\Gamma(t)}{1+\epsilon|\Gamma(t)|^2}. \tag{4.9}$$

In this expression, $\epsilon = \frac{1}{4\Gamma^2_{(max)}}$ where $\Gamma_{(max)}$ specifies the maximum weight that a trajectory can have. The exact, non-damped expression will be recovered in the limit that $\Gamma_{(max)} \to \infty$, so by increasing $\Gamma_{(max)}$, the correct result can be approached asymptotically. Figure 4.4 shows how $\Gamma^{(\epsilon)}$ depends on $\Gamma$ for different values of $\Gamma_{(max)}$. For small values of $\Gamma$, $\Gamma^{(\epsilon)}(0) \simeq \Gamma$ but as $\Gamma$ increases, $\Gamma^{(\epsilon)}$ grows less rapidly and reaches a peak height of $\Gamma_{(max)}$, before tending back towards 0. We choose to stop running any trajectories for which $|\Gamma^{\epsilon}(t)| < \frac{1}{\Gamma_{(max)}}$ as they will contribute negligibly to the sum.

## 4.5 Semiclassical Results

It was found that FGA-SH simulations using the branching algorithm were unable to converge either autocorrelation function with any reasonable number of trajectories. Instead, $C(t)$ was seen to explode to values much greater than 1 even at short times. The reason for this can be seen in Figure 4.5 where the number of trajectories ,$M(t)$, against time for the simulation of the $S_2$ spectrum is plotted.

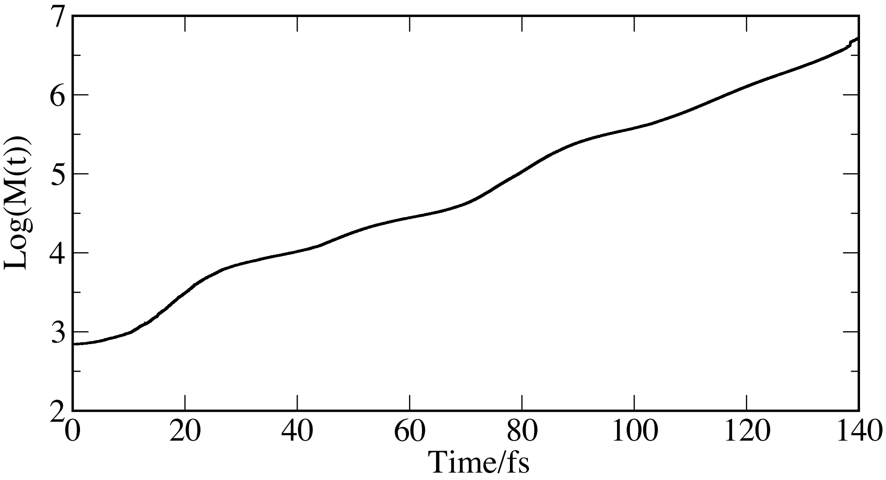

**Figure 4.5** The logarithm of the number of trajectories $M(t)$ against time for simulation of the $S_2$ spectrum when computed using the branching algorithm. $M(0) = 700$

Figure 4.5 shows that the branching of trajectories leads to an exponential increase in their number through time. Since we require at least $10^6$ trajectories to accurately describe the initial wavefunction, this growth will necessitate the propagation of many billions of trajectories to converge the $S_2$ spectrum, which is not feasible.

This problem was not exhibited in simple avoided crossing simulations performed using FGA-SH[18], where instead $M(t)$ scaled in an approximately linear fashion with $t$. This is because pyrazine is non-dissociative, so the trajectories never leave the interaction region. Thus, they will continue to pick up larger values of $\omega(t)$ through time, leading to exponential growth of $M(t)$. From this, it appears that the branching algorithm is not suitable for the majority of chemical systems in the nonadiabatic regime.

Attempts were made to simulate both $S_1$ and $S_2$ autocorrelation functions $C_1(t)$ and $C_2(t)$ with FGA-SH using the prefactor damping algorithm. In contrast to the branching algorithm, it was possible to obtain converged results. The results were converged with respect to both the number of trajectories and the time step, $\Delta t$ for each value of $\Gamma_{(max)}$. A time step of $\Delta t = 4$a.u, was found to be appropriately small to converge the results. The autocorrelation functions were then damped with an exponential decay function,

$$\tilde{C}_j(t) = C_j(t)e^{\frac{-t}{T_{2j}}} \tag{4.10}$$

in order to match the phenomenological widths observed in experiment. This is exactly equivalent to the Lorentzian transform of the simulated stick spectra in section 4.3, and uses same decay constants, $T_{2_1} = 500\,\text{fs}$ and $T_{2_2} = 30\,\text{fs}$. The semiclassical absorption spectra was then generated by performing a Fourier transform on the damped autocorrelation functions,

$$I_j(E) = \text{Re}\frac{1}{\pi}\int_0^\infty e^{iEt}\tilde{C}_j(t)dt. \tag{4.11}$$

### 4.5.1 $S_1$ Spectrum

The semiclassical results for the $S_1$ spectrum are shown for $\Gamma_{(max)} = 50$ and $\Gamma_{(max)} = 5000$ in Figure 4.6. As $\Gamma_{(max)}$ is increased, the widths of the peaks can be seen to become narrower and the details better resolved. However, as the average weight of the trajectories has also increased, it is necessary to sample over a larger number to converge the correlation function. For $\Gamma_{(max)} = 50$, the initial number of trajectories required, $M(0)$, was $1.6 \times 10^6$ whereas for the highest value, $\Gamma_{(max)} = 5000$, $M(0) = 1.4 \times 10^8$. The FGA-SH simulated $S_1$ spectrum was seen to converge with respect to $\Gamma_{(max)}$ for $\Gamma_{(max)} = 5000$. This is compared to the quantum mechanical simulation in Figure 4.7, where it shows an excellent quantitative agreement, with nearly all the details precisely reproduced in the semiclassical simulation.

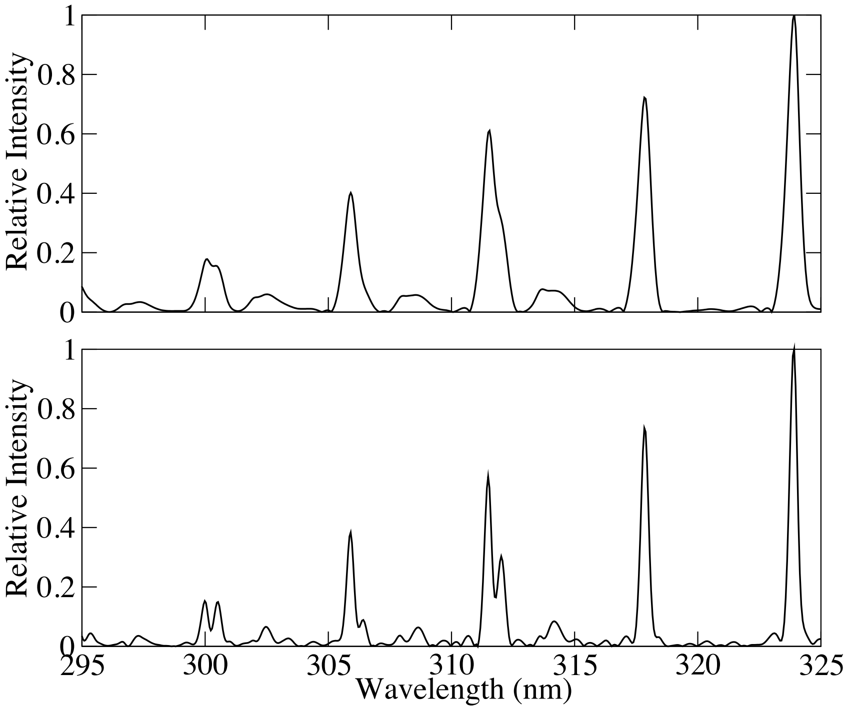

**Figure 4.6** Simulated $S_1$ absorption spectra for $\Gamma_{(max)}$ = 50, (upper panel) and $\Gamma_{(max)}$ = 5000, (lower panel) for the 4-mode model of pyrazine.

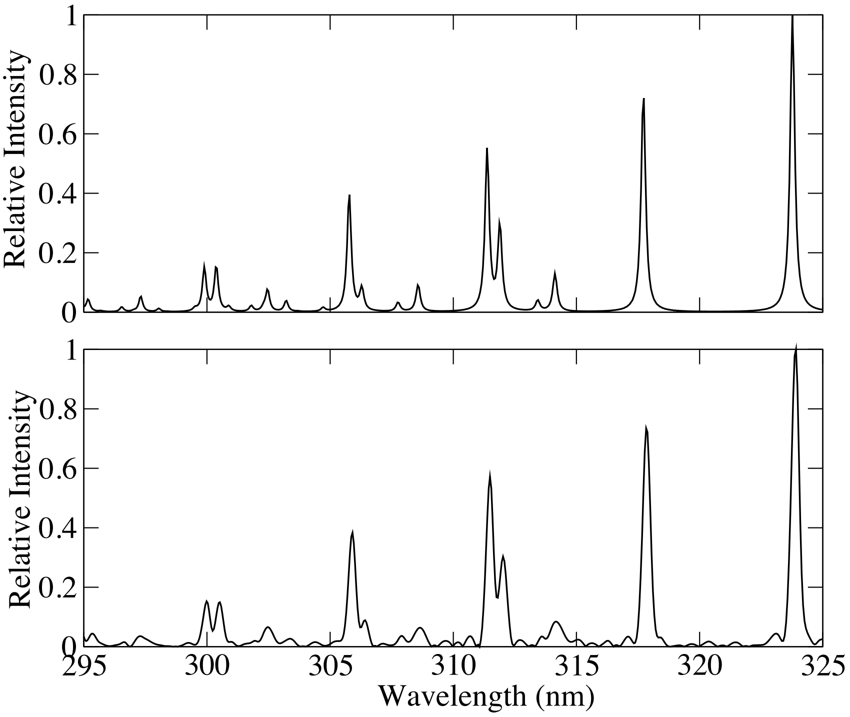

**Figure 4.7** Comparison of the $S_1$ absorption spectrum simulated by quantum calculation (upper panel) and the FGA-SH result with $\Gamma_{(max)}$ = 5000, (lower panel) for the 4-mode model of pyrazine.

### 4.5.2 $S_2$ Spectrum

The results for the $S_2$ spectrum with $\Gamma_{(max)} = 50$ and $\Gamma_{(max)} = 5000$ are shown in Figure 4.8. We see that even for $\Gamma_{(max)} = 50$, most of the shape of the $S_2$ spectrum is correctly reproduced. In 4.9, the converged FGA-SH result, which required $\Gamma_{(max)} = 5000$ is compared to the quantum spectrum. It can be seen that, similar to the $S_1$ simulation, there is a very good agreement between the spectra. This shows that the FGA-SH method can be used to calculate accurate vibronic absorption spectra once the results are converged with respect to the parameter $\Gamma_{(max)}$ in the prefactor damping algorithm.

### 4.5.3 Discussion

The effect that increasing the value of $\Gamma_{(max)}$ has on simulation can be better visualised by plotting the absolute values of the $S_1$ correlation functions for different values of $\Gamma_{(max)}$, which is done in Figure 4.10. We see that, compared to the quantum result, the semiclassical autocorrelation functions are damped through time, with the fastest damping seen for the smallest values of $\Gamma_{(max)}$.

The reason for this damping can be seen by tracking the fraction of the trajectories that remain in simulation through time, which is done in Figure 4.11. The prefactor damping algorithm removes trajectories for which $|\Gamma^{\epsilon}(t)| < \frac{1}{4\Gamma_{(max)}}$, which corresponds to trajectories for which the undamped $\Gamma(t)$ would be larger than $4\Gamma^3_{(max)}$. By increasing $\Gamma_{(max)}$, we increase the tolerance for larger trajectories, so a larger number remain in simulation over a given period of time. The fact that the autocorrelation function is damped shows that the assumption that trajectories with large weights will cancel each other becomes less true over time, with the large trajectories being required for accurate determination of the integrand.

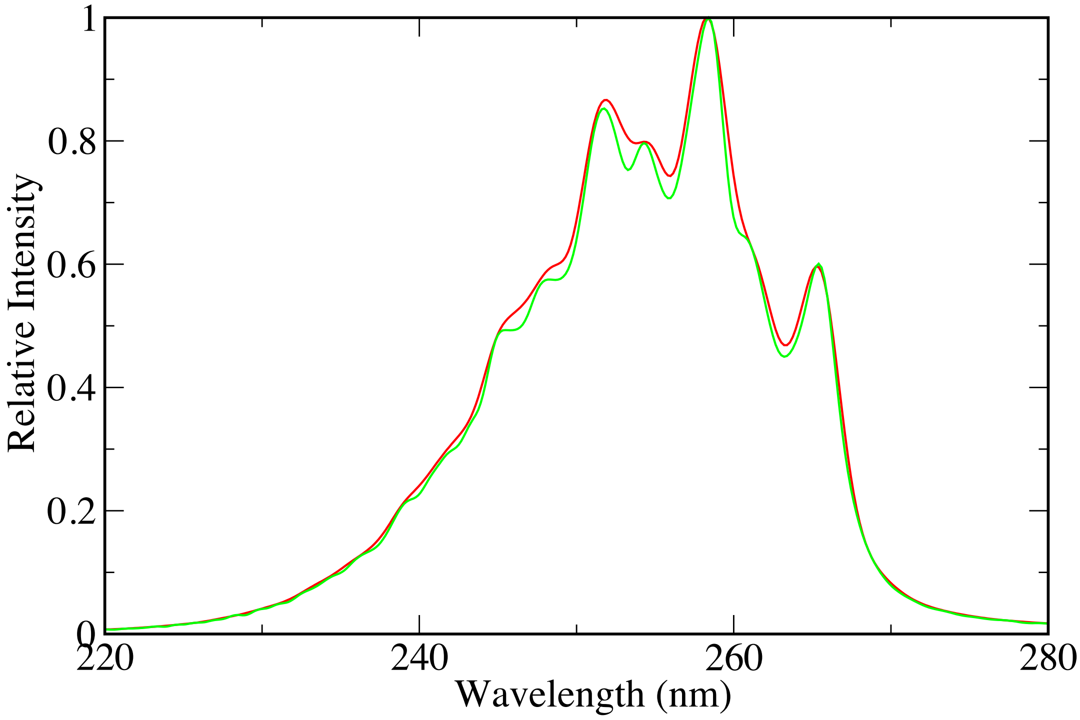

**Figure 4.8** Simulated $S_2$ absorption spectra for $\Gamma_{(max)} = 50$, (red) and $\Gamma_{(max)} = 5000$, (green) for the 4-mode pyrazine model.

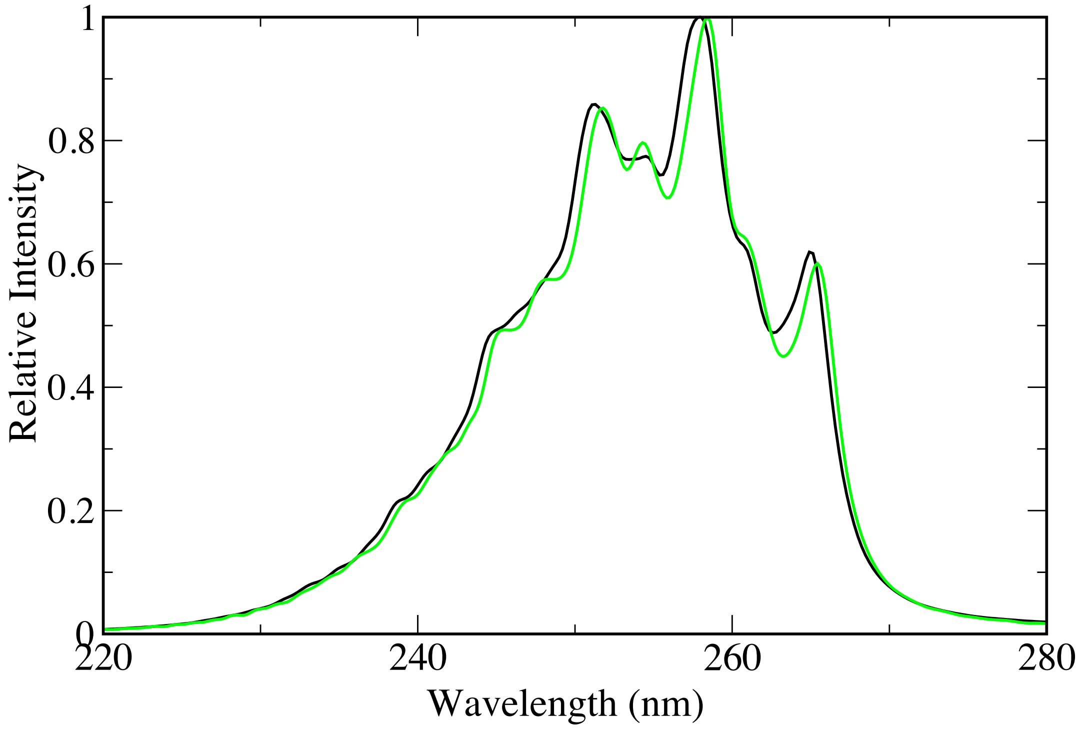

**Figure 4.9** Comparison of the $S_2$ absorption spectrum simulated by quantum calculation (black) and the FGA-SH result with $\Gamma_{(max)} = 5000$, (green) for the 4-mode pyrazine model.

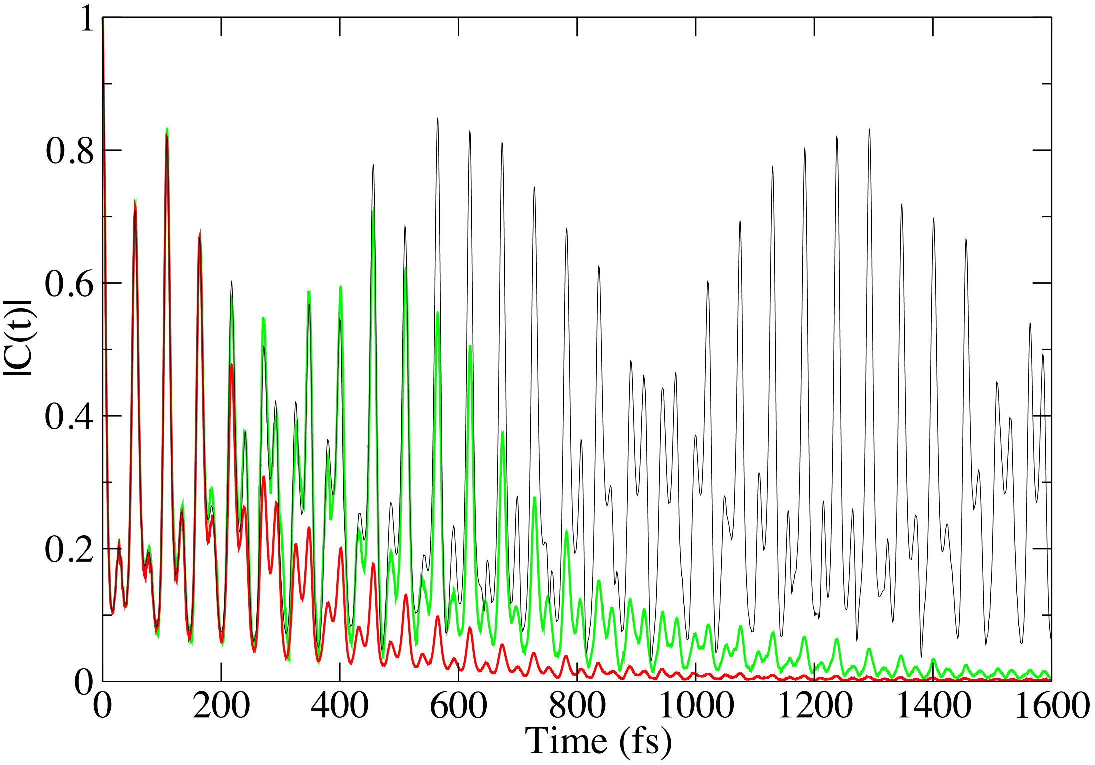

**Figure 4.10** The absolute value of the simulated $S_1$ autocorrelation function, $|C_1|(t)$, for $\Gamma_{(max)} = 50$ (Red) and $\Gamma_{(max)} = 5000$ (Blue), compared to the quantum simulation (Black) for the 4-mode pyrazine model.

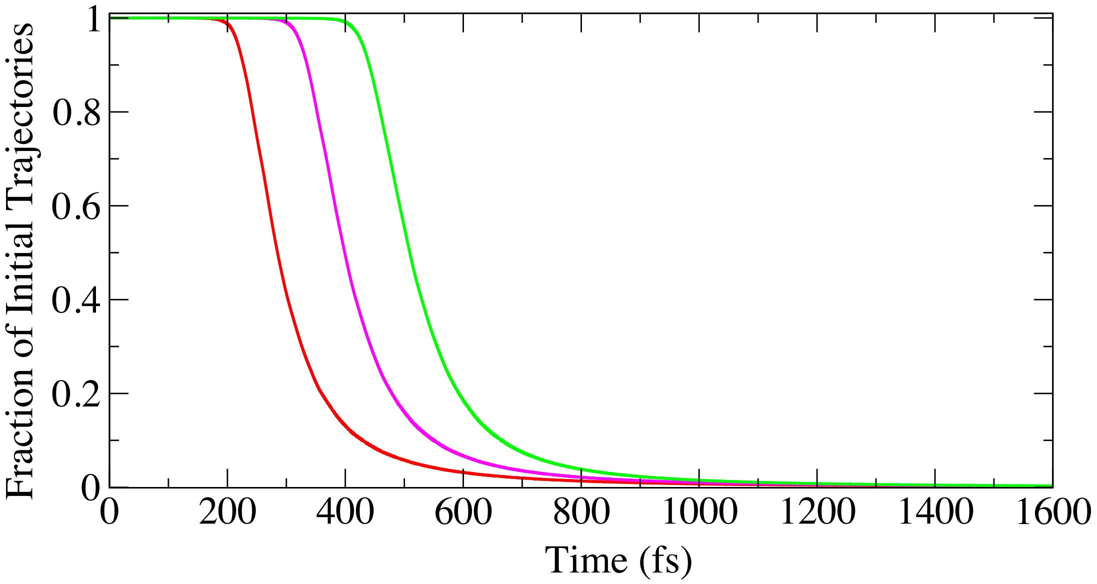

**Figure 4.11** The fraction of initial trajectories, $\frac{M(t)}{M(0)}$ as a function of time for different values of $\Gamma_{(max)}$. $\Gamma_{(max)} = 50$ (Red), $\Gamma_{(max)} = 500$ (Magenta), and $\Gamma_{(max)} = 5000$ (Green) for the 4-mode pyrazine model.

## Chapter 5

# The 24-mode Pyrazine Model

Following the success of the FGA-SH method in producing accurate absorption spectra for the 4-mode pyrazine problem, simulations were carried out on a fully parametrised Hamiltonian that takes into account all 24-modes, introduced by Raab. et al[21]. As this contains all of the nuclear modes, it should correctly account for any damping of the autocorrelation function due to intrastate vibrational relaxation.

The size of the 24-mode system is not possible to treat in a straightforward way as was done for the 4-mode model. Thus, a semiclassical method that can handle systems of this size would show significant promise for simulation of nonadiabatic dynamics. A full ab initio 24-mode pyrazine model has been parametrised by Raab et al. The symmetries of the modes are presented in table 5.1.

| | Mode | Symmetry | | Mode | Symmetry | | Mode | Symmetry |
|---|---|---|---|---|---|---|---|---|
| 1 | $\nu_{10a}$ | $\Gamma_{B_{1g}}$ | 9 | $\nu_{6b}$ | $\Gamma_{B_{3g}}$ | 17 | $\nu_{19a}$ | $\Gamma_{B_{1u}}$ |
| 2 | $\nu_1$ | $\Gamma_{A_g}$ | 10 | $\nu_3$ | $\Gamma_{B_{3g}}$ | 18 | $\nu_{13}$ | $\Gamma_{B_{1u}}$ |
| 3 | $\nu_2$ | $\Gamma_{A_g}$ | 11 | $\nu_{8b}$ | $\Gamma_{B_{3g}}$ | 19 | $\nu_{18b}$ | $\Gamma_{B_{2u}}$ |
| 4 | $\nu_{6a}$ | $\Gamma_{A_g}$ | 12 | $\nu_{7b}$ | $\Gamma_{B_{3g}}$ | 20 | $\nu_{14}$ | $\Gamma_{B_{2u}}$ |
| 5 | $\nu_{8a}$ | $\Gamma_{A_g}$ | 13 | $\nu_{16a}$ | $\Gamma_{A_u}$ | 21 | $\nu_{19b}$ | $\Gamma_{B_{2u}}$ |
| 6 | $\nu_{9a}$ | $\Gamma_{A_g}$ | 14 | $\nu_{17a}$ | $\Gamma_{A_u}$ | 22 | $\nu_{20b}$ | $\Gamma_{B_{2u}}$ |
| 7 | $\nu_4$ | $\Gamma_{B_{2g}}$ | 15 | $\nu_{12}$ | $\Gamma_{B_{1u}}$ | 23 | $\nu_{16b}$ | $\Gamma_{B_{3u}}$ |
| 8 | $\nu_5$ | $\Gamma_{B_{2g}}$ | 16 | $\nu_{18a}$ | $\Gamma_{B_{1u}}$ | 24 | $\nu_{11}$ | $\Gamma_{B_{3u}}$ |

**Table 5.1** The symmetries of the 24 vibrational normal modes in pyrazine

## 5.1 Model Hamiltonian

The Hamiltonian of Raab et al. retains all on- and off- diagonal terms up to second order. It can be written in the same form as Equation (4.1) to give:

$$
\begin{aligned}
\mathcal{H} = {} & \left( \sum_{i}^{24} \frac{\omega_i}{2} \left( -\frac{\partial^2}{\partial q_i^2} + q_i^2 \right) \right) \hat{\mathbf{1}} + \begin{pmatrix} -\Delta & 0 \\ 0 & \Delta \end{pmatrix} + \sum_{i \in G_1} \begin{pmatrix} \kappa_i^{(1)} & 0 \\ 0 & \kappa_i^{(2)} \end{pmatrix} \mathrm{q}_i + \sum_{(i,j) \in G_2} \begin{pmatrix} \gamma_{i,j}^{(1)} & 0 \\ 0 & \gamma_{i,j}^{(2)} \end{pmatrix} \mathrm{q}_i \mathrm{q}_j \\
& + \sum_{i \in G_3} \begin{pmatrix} 0 & \lambda_i^{(1)} \\ \lambda_i^{(2)} & 0 \end{pmatrix} \mathrm{q}_i + \sum_{(i,j) \in G_4} \begin{pmatrix} 0 & c_{i,j} \\ c_{i,j} & 0 \end{pmatrix} \mathrm{q}_i \mathrm{q}_j
\end{aligned}
\tag{5.1}
$$

The first term is of the same form as $\mathcal{H}_0$ in Equation (4.1), describing the ground state in the harmonic approximation, except that for now it is extended over all 24-modes. The second term accounts for the difference in energy between the $S_1$ and $S_2$ electronic states. No reference is made to the energy difference between them and the ground state, so this parameter was empirically chosen to match the spectra to experiment.

The third and fourth terms have the same form as the linear $\kappa$ and quadratic $\gamma$ terms that appear in the 4-mode model. Since each element of $\mathcal{H}$ must have $\Gamma_{A_g}$ symmetry, each term in Equation (5.1) is a sum over a group of modes, $G_i$, that have the required symmetries. It can be shown that the group $G_1$ will contain only the modes that have $\Gamma_{A_g}$ symmetry while $G_2$ contains terms only for the pairs of modes for which $\Gamma_i \otimes \Gamma_j = A_g$. The fifth term contains a group $G_3$ of off-diagonal linear terms. In section 4 we have shown that there is only one mode in this group: the $B_{1g}$ symmetry $\nu_{10a}$ mode. The last term contains quadratic off-diagonal elements, which due to their small magnitude were entirely neglected in the 4-mode model. They contain pairs of modes for which $\Gamma_i \otimes \Gamma_j = B_{1g}$.

In total there are 102 parameters that feature in $\mathcal{H}$. A complete set of these is provided in Appendix B.

## 5.2 MCTDH Simulation

As discussed at the beginning of Chapter 4, writing the full Hamiltonian in a basis set that takes into account all relevant vibrational states is not possible. Thus, in order to calculate spectra, Raab et al. employed the faster but more approximate Multi-Configurational Time Dependent Hartree, (MCTDH), method which reduces the size of the Hilbert space by approximating the wavefunction in a smaller basis set.

Although all intrastate vibrational relaxation should now be accounted for by inclusion of the twenty other modes, additional broadening will still be seen in the experimental spectra. This is due to unresolved rotational structure which is not accounted for in the model, and also to the systematic time-energy uncertainty from the experimental technique. Thus, for the MCTDH result, a weaker phenomenological damping function was employed for the $S_2$ spectrum, with a damping constant increased from $T_2 = 30\,\text{fs}$ to $T_2 = 150\,\text{fs}$. A Hamming window was also used in order to reduce ringing, which is the occurrence of spurious artefacts in the spectrum from taking the discrete Fourier transform of a finite autocorrelation function that is incompletely damped. To do this, $C(t)$ is multiplied by $g(t)$ where

$$g(t) = cos\left(\frac{\pi t}{2T}\right), \tag{5.2}$$

and $T$ is the total time period over which the simulation has been run. The resulting MCTDH spectrum is compared with the experimental $S_2$ absorption spectrum in Figure 5.1. It shows very good agreement, reproducing the width and key features. The MCTDH calculation does however exhibit some spurious structure, including a peak at $\sim 262\,\text{nm}$ and some oscillatory artefacts at high wavelength. Raab et al. attributed these discrepancies to the limited accuracy of the parameters.[21] Therefore, we will compare our FGA-SH simulations with the MCTDH calculation to eliminate the systematic error in the model.

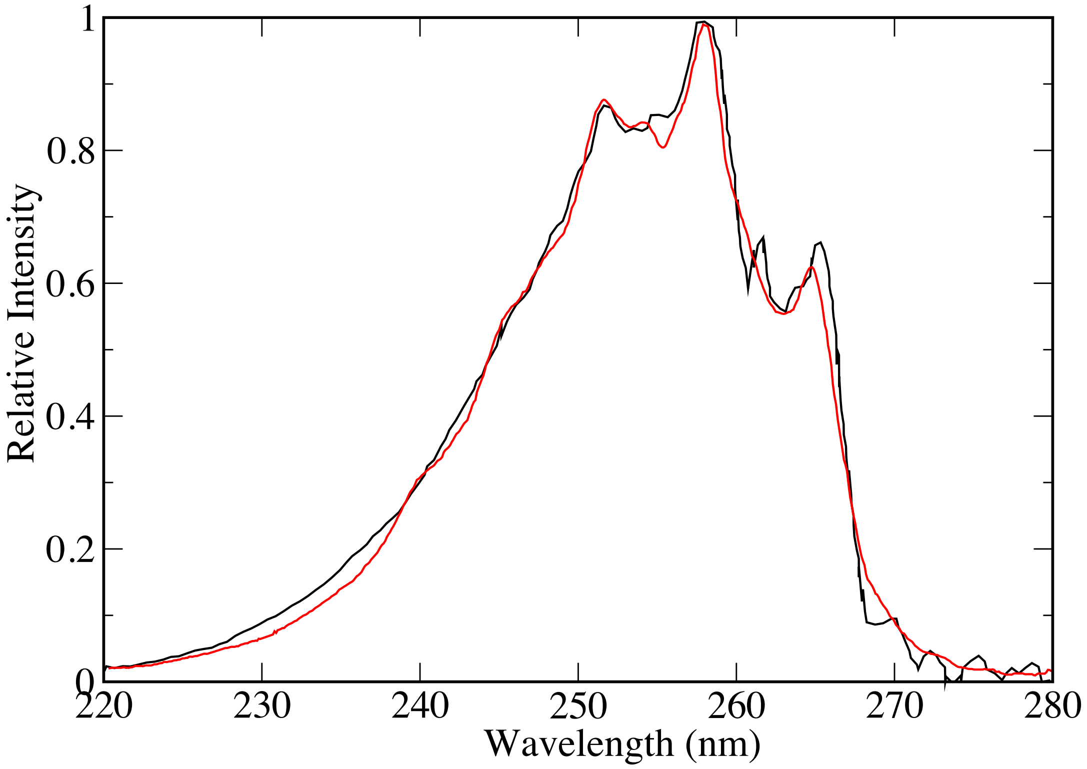

**Figure 5.1** Comparison of the $S_2$ spectrum obtained by MCTDH[21] (black) with the experimental result[26] (red) for the full 24-mode pyrazine model.

## 5.3 Semiclassical Results

The $S_1$ and $S_2$ spectra were simulated using the FGA-SH method with the prefactor damping algorithm for the 24-mode Hamiltonian. It was found possible to converge both with values of $\Gamma_{(max)} = 500$. This required $\sim 1.8 \times 10^8$ trajectories to converge the $S_2$ spectrum, which compares to $6.2 \times 10^7$ in the 4-mode simulations.

### 5.3.1 $S_2$ Spectrum

The spectrum for $\Gamma_{(max)} = 500$ is compared to the MCTDH simulation in Figure 5.2. Since the excitation energy from $S_0$ to the $S_1/S_2$ adiabats is not included in the model Hamiltonian, the simulated spectra have been aligned with experiment, with a vertical excitation energy of $E_v = 4.0817$ eV.

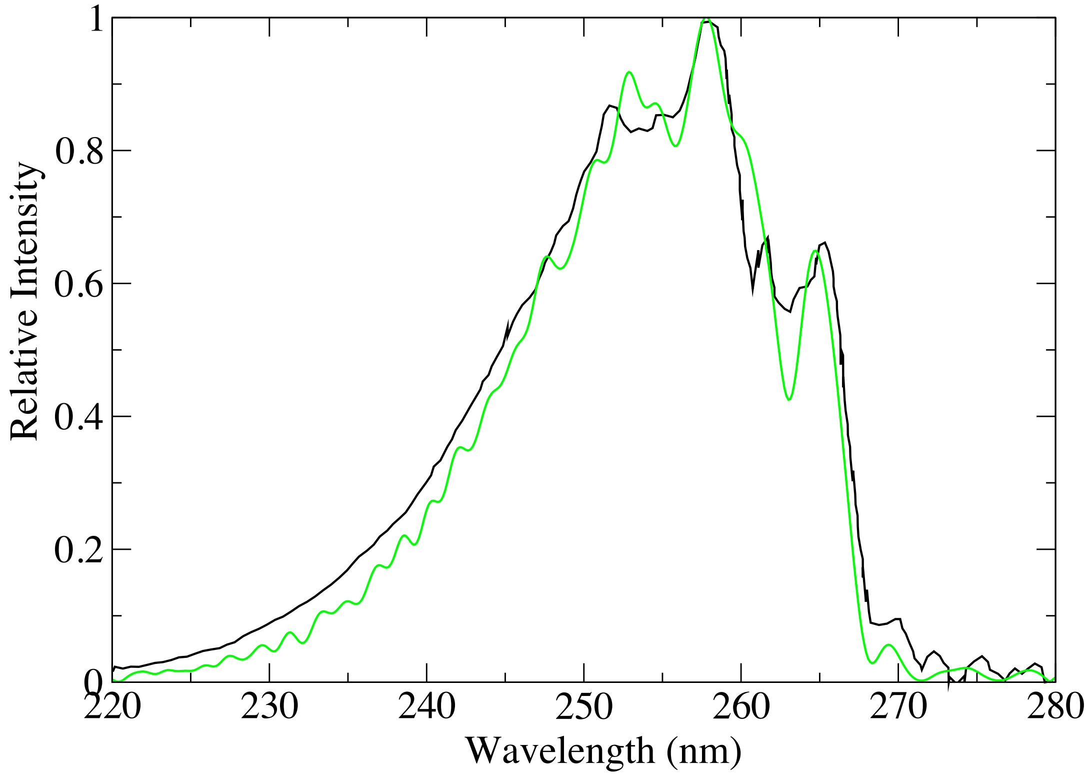

**Figure 5.2** Comparison of the $S_2$ absorption spectrum simulated by MCTDH[21] (black) with the FGA-SH result for $\Gamma_{(max)} = 500$, (green) for the full 24-mode pyrazine model.

It can be seen that the spectral envelopes of FGA-SH and MCTDH simulations of the $S_2$ spectrum are of similar widths, indicating that the broadening effect of the additional twenty Franck Condon inactive modes is correctly accounted for in the semiclassical treatment. The spectra show qualitative agreement in the location of the principal peaks, but intensities and positions in the FGA-SH simulation are not quantitatively correct, especially at higher frequencies. This discrepancy is also seen in another semiclassical approach, which used a mapping-variable technique with Filinov smoothing to simulate the $S_2$ spectrum from the same parameter set.[45] Both methods exhibit the spurious oscillatory structure around the tail region at 230 – 250 nm and do not give quantitative agreement with the MCTDH peak positions and intensities. It is possible that in the FGA-SH method, this could be improved by using a larger value of $\Gamma_{(max)}$, which would require the propagation of more trajectories than was feasible in this work.

### 5.3.2 $S_1$ Spectrum

Previous studies of the 24-mode Hamiltonian have only focussed on the $S_2$ region, presumably because the model parameters are optimised only for the $S_2$ surface.[21] This means that there is not a suitable reference with which to make comparison. However, for completeness, and for future comparisons, we include the simulated $S_1$ absorption spectrum for the 24-mode model with $\Gamma_{(max)} = 500$ in Figure 5.3.

To reproduce the line-widths of the experimental spectrum in 1.4, it was found to be unnecessary to use any phenomological damping constant. An interesting feature in Figure 5.3 is the presence of a peak at around 321 nm. This is in a similar position to the $10a^1$ peak seen experimentally in Figure 1.4. This is not seen in the $S_1$ spectrum of the 4D model (upper panel of Figure 4.2) as none of the terms in the 4-mode Hamiltonian have the correct symmetry. However, the quadratic off-diagonal coupling terms in Equation (5.1) permit $10a^1$ excitations to occur on the $S_1$ surface.

## 5.4 Scaling

As the dimensionality of the phase space in the 24-mode model is much larger, it requires greater sampling over the initial positions $(\mathbf{p}_0, \mathbf{q}_0)$ to accurately describe the wavefunction and therefore more trajectories for a given $\Gamma_{(max)}$. It interesting to also consider the fractional number of trajectories for each Hamiltonian as a function of time, which we plot in Figure 5.4. In this comparison, we have included simulations for $\Gamma_{(max)} = 5000$ for the 24-mode model which, although the autocorrelation function could not be converged, the fraction of trajectories as a function of time could be established. It can be seen that the trajectories are more rapidly removed from the simulation in the 24-mode model, which indicates that $\Gamma(t) = R(t)e^{\omega(t)}$ grows faster as a function of time. This shows a possible limitation for the use of FGA-SH with prefactor damping: as the number of nuclear degrees of freedom within the model increases, a larger value of $\Gamma_{(max)}$ (and hence more trajectories) will be required for convergence.

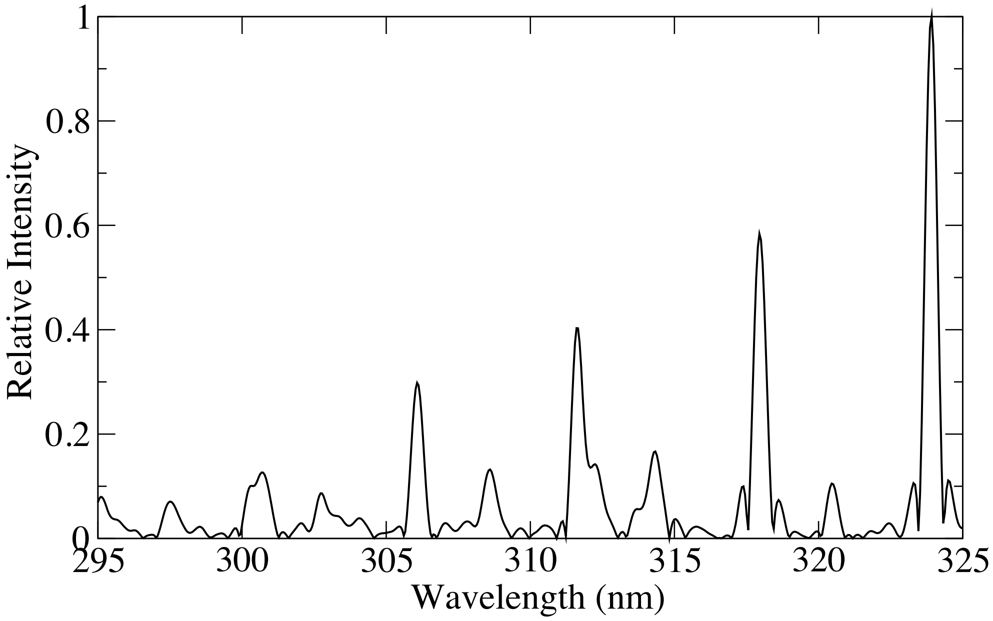

**Figure 5.3** The $S_1$ absorption spectrum obtained with FGA-SH for $\Gamma_{(max)} = 500$ for the full 24-mode pyrazine model.

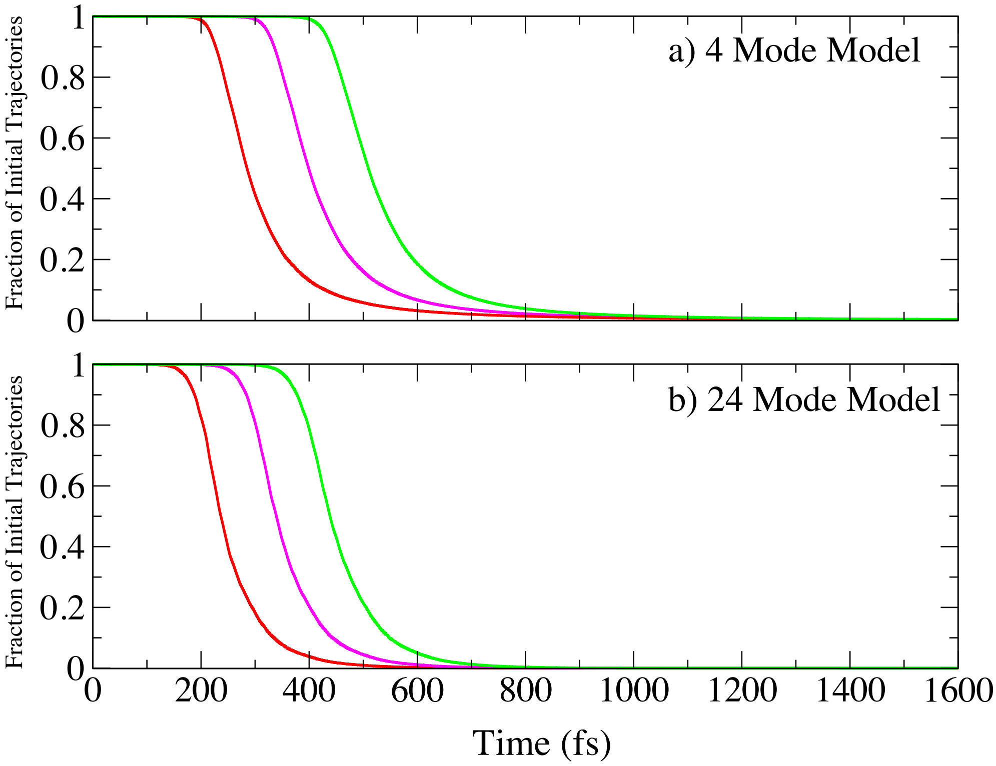

**Figure 5.4** A comparison of the fraction of trajectories that remain as a function of time for FGA-SH simulations of both 4 and 24-mode systems. $\Gamma_{(max)} = 50$ (Red), $\Gamma_{(max)} = 500$ (Magenta), and $\Gamma_{(max)} = 5000$ (Green).

## Chapter 6

# Conclusions and future work

## 6.1 Conclusions

In this thesis, a theory for modelling dynamics in the nonadiabatic regime, which combines the semiclassical Frozen Gaussian Approximation with a stochastic surface hopping algorithm, has been used to simulate the absorption spectrum of pyrazine. To achieve this, an algorithm based on Filinov smoothing was developed in order to improve convergence issues related to oscillatory nature of the FGA-SH integrand. The method was tested on a reduced dimensionality 4 mode model of pyrazine, where it showed excellent agreement with exact quantum mechanical calculations. Absorption spectra for the full 24 mode pyrazine molecule were also simulated, and found to give qualitative agreement between FGA-SH and MCTDH calculations.

## 6.2 Future work

The FGA-SH method has many potential future applications. One area of interest is the unimolecular decomposition of acetaldehyde, $H_3CCHO$ into $CH_4$ and CO. This can take place through a number of competing mechanisms that lead to different rotationally excited products. One, the so-called 'roaming' mechanism, involves a $\cdot CH_3$ radical exploring a large amount of the energy surface before abstracting a hydrogen atom[46]. The dynamics of this mechanism involves three interacting electronic surfaces and 15 nuclear degrees of freedom which presents a system too large for exact quantum calculation. The trajectory-based approach in FGA-SH would be particularly useful to treat this problem, as methods like MCTDH and FMS would require large quantum mechanical basis sets to describe the roaming pathway.

# References

[1] A. W. Jasper, C. Zhu, S. Nangia, D. G. Truhlar, *Faraday Discuss. Chem. Soc.* **2004**, *127*, 1–22.

[2] M. H. Beck, A. Jäckle, G. A. Worth, H.-D. Meyer, **2012**.

[3] M. Karplus, J. Kuriyan, *Proceedings of the National Academy of Sciences* **2005**, *102*, 6679–6685.

[4] J. D. McGeagh, K. E. Ranaghan, A. J. Mulholland, *Biochimica and Biophysica Acta - Proteins and Proteomics* **2011**, *1814*, 1077–1092.

[5] A. J. Cohen, P. Mori-Sanchez, W. Yang, *Chemical Reviews* **2012**, *112*, 289–320.

[6] E. Engel, S. Keller, A. F. Bonetti, H. Muller, R. M. .Dreizler, *Physical Review A* **1995**, *52*, 2750.

[7] I. R. Craig, D. E. Manolopoulos, *Journal of Chemical Physics* **2004**, *121*, 3368.

[8] T. F. Miller, D. E. Manolopoulos, *Journal of Chemical Physics* **2005**, *123*, 154504.

[9] E. Kluk, M. F. Herman, H. L. Davis, *American Institute of Physics* **1986**, *84*, 326 –334.

[10] K. G. Kay, *Annual Review of Physical Chemistry* **2005**, *56*, 255–280.

[11] W. Domcke, D. Yarkony, H. Köppel, *Conical Intersections: Theory, Computation and Experiment*, Advanced Series in Physical Chemistry, **2011**.

[12] S. Meng, E. Kaxiras, *Journal of Biophysics* **2008**, *95*, 4396–4402.

[13] S. Ullrich, T. Schultz, M. Z. Zgierskia, A. Stolow, *Physical Chemistry Chemical Phyiscs* **2003**, *6*.

[14] T. J.Martinez, M. Ben-Nun, R. D. Levine, *Journal of Chemical Physics* **1996**, *100*, 7884–7895.

[15] J. C. Tully, *Journal of Chemical Physics* **1990**, *93*, 1061.

[16] J. E. Subotnik, N. Shenvi, *Journal of Chemical Physics* **2011**, *134*, 244114.

[17] M. Thoss, G. Stock, *Physical Review A* **1999**, *59*, 64.

[18] J Lu, Z Zhou, *Journal of Chemical Physics* **2016**, *142*, 124109.

[19] C. Lasser, T. Swart, *Journal of Chemical Physics* **2008**, *129*, 034302.

[20] M. Thoss, W. H. Miller, G. Stock, *Journal of Chemical Physics* **2000**, *112*, 10282.

[21] A. Raab, G. A. Worth, H.-D. Meyer, L. S. Cederbaum, *Journal of Chemical Physics* **1999**, *110*, 936.

[22] D. R. Yarkony, *Acc. Chem. Res.* **1998**, *31*, 511–518.

[23] *Glossary of terms used in photochemistry, 3rd edition*, IUPAC, **2006**.

[24] C. Woywod, W. Domcke, A. L. Sobolewski, H. Werner, *American Institute of Physics* **1993**, *100*, 1400–1413.

[25] K. Yamanouchi, S. Cundiffand, R. de Vivie-Riedle, M. Kuwata-Gonokami, L. DiMauro, Eds., Ab Initio Quantum Dynamical Study on Ultrafast Nonradiative Transition Pathways of Pyrazine, *Vol. Vol 162*, Ultrafast Phenomena XIX. Springer Proceedings in Physics 162, Springer Proceedings in Physics, **2014**.

[26] I. Yamazaki, T. Murao, T. Yamanaka, K. Yoshihara, *Farady Discuss. Chem. Soc.* **1982**, *75*, 395–405.

[27] M. E. Tuckerman, *p.30 Statistical Mechanics: Theory and Molecular Simulation*, Oxford Graduate Texts, **2010**.

[28] R. P. Feynman, A. R. Hibbs, *p. 44 Quantum Mechanics and Path Integrals*, McGraw-Hill, **1965**.

[29] S. A. Albeverio, R. J. Høegh-Krohn, S. Mazzucchi, *p 108 Mathematical Theory of Feynman Path Integrals*, Springer, **2008**.

[30] M. F. Herman, E. Kluk, *Chemical Physics* **1984**, *91*, 27–34.

[31] K. G. Kay, *Chemical Physics* **2005**, *322*, 3–12.

[32] R. J. Glauber, *Physical Review* **1963**, *131*, 2766.

[33] M. Ceotto, S. Atahan, G. F. Tantardini, A. Aspuru-Guzik, *Journal of Chemical Physics* **2009**, *130*, 234113.

[34] M. L. Brewer, J. S. Hulme, D. E. Manolopoulos, *Journal of Chemical Physics* **1997**, *106*, 4832.

[35] M. Born, K. Huang, *p. 406 Dynamical Theories of Crystal Lattices*, Oxford University Press, **1954**.

[36] J. Lu, Z. Zhou, "Frozen Gaussian Approximation with Surface Hopping for Mixed Quantum-Classical Dynamics: A Mathematical Justification of Fewest Switches Surface Hopping Algorithms", **2016**.

[37] T. Swart, V. Rousse, *Communications in Mathematical Phyiscs* **2008**, *286*, 725–750.

[38] I. R. Craig, MA thesis, Oxford University, **2002**.

[39] K. K. Innes, I. G. Ross, W. R. Moomaw, *Journal of Molecular Spectroscopy* **1988**, *132*, 492–544.

[40] R. Berger, C. Fischer, M. Klessinger, *Journal of Chemical Physics* **1998**, *102*, 7157–7167.

[41] A. R. Walton, D. E. Manolopoulos, *Molecular Physics* **1996**, *87*, 961–978.

[42] K. G. Kay, *Journal of Chemical Physics* **1994**, *101*, 2250.

[43] E. J. Heller, *Journal of Chemical Physics* **1991**, *94*, 2723.

[44] H. Wang, D. E. Manolopoulos, W. H. Miller, *Journal of Chemical Physics* **2001**, 6317.

[45] M. Thoss, W. H. Miller, G. Stock, *Journal of Chemical Physics* **2000**, *112*, 10282.

[46] B. R. Heazlewood, M. J. T. Jordan, S. H. Kable, T. M. Selby, D. L. Osborn, B. C. Shepler, B. J. Braams, J. M. Bowman, *Proceedings of the National Academy of Sciences* **2008**, *105*, 12719–12724.

[47] A. M. O. de Almeida, *p 194 Hamiltonian Systems, Chaos and Quantization*, Cambridge University Press, **1990**.

# Appendices

## Appendix A

# The Hermann-Kluk Prefactor

In this appendix, we show that the complex pre-factor $A(t)$ which appears in the original derivation of FGA-SH by Lu and Zhou[18], satisfies the same equation of motion as the Herman-Kluk prefactor for singlet systems in the absence of a magnetic field.

The evolution of $A(t)$ is described by the differential equation,

$$\dot{A}(t) = \frac{A(t)}{2}\mathrm{tr}\left(\frac{\mathbf{M_{pq}} - i\mathbf{M_{pp}} - \nabla^2_{\mathbf{x}}V(\mathbf{q})(i\mathbf{M_{qq}} + \mathbf{M_{qp}})}{\mathbf{M_{pp}} + i\mathbf{M_{pq}} - i\mathbf{M_{qp}} + \mathbf{M_{qq}}}\right) - A(t)\mathbf{p}_t \cdot \mathbf{d}_{ll}(\mathbf{q}_t). \tag{A.1}$$

The second term in the equation contains a diagonal element of the derivative coupling matrix which, from (2.23), is given by:

$$\mathbf{d}_{ll}(\mathbf{x}) = \int \chi_l^*(\mathbf{x};\mathbf{r})\frac{\partial \chi_l(\mathbf{x};\mathbf{r})}{\partial \mathbf{x}}\mathrm{d}\mathbf{x} \tag{A.2}$$

Integrating by parts, we get that

$$\int \chi_l^*(\mathbf{x},\mathbf{r})\frac{\partial \chi_l(\mathbf{x};\mathbf{r})}{\partial \mathbf{x}}\mathrm{d}\mathbf{x} = [\chi_l^*(\mathbf{x};\mathbf{r})\chi_l(\mathbf{x};\mathbf{r})] - \int \chi_l(\mathbf{x},\mathbf{r})\frac{\partial \chi_l^*(\mathbf{x};\mathbf{r})}{\partial \mathbf{x}}\mathrm{d}\mathbf{x}, \tag{A.3}$$

and taking the first term on the right to be zero, as the wavefunction must vanish as $|\mathbf{x}| \to \infty$, gives

$$\mathbf{d}_{ll}(\mathbf{x}) = -\mathbf{d}_{ll}^*(\mathbf{x}), \tag{A.4}$$

which shows that $\mathbf{d}_{ll}$ is a purely imaginary quantity. Furthermore, for singlet systems in the absence of a magnetic field such as the pyrazine model considered in this thesis, time-reversal symmetry dictates that the electronic Hamiltonian, $\hat{H}_e$ is real symmetric.[47] This means that the electronic wavefunction, an eigenvalue of $H_e$, will be real, and therefore that $\mathbf{d}_{ll}(\mathbf{x}) = \mathbf{d}^*_{ll}(\mathbf{x}) = 0$. In these cases, the second term in (A.1) will be exactly 0 for all time.

Letting $\Lambda(t) = \mathbf{M_{pp}} + i\mathbf{M_{pq}} - i\mathbf{M_{qp}} + \mathbf{M_{qq}}$ and substituting for the derivatives of the monodromy matrix,

$$\dot{\mathbf{M}} = \begin{pmatrix} \dot{\mathbf{M}}_{\mathbf{pp}} & \dot{\mathbf{M}}_{\mathbf{pq}} \\ \dot{\mathbf{M}}_{\mathbf{qp}} & \dot{\mathbf{M}}_{\mathbf{qq}} \end{pmatrix} = \begin{pmatrix} -\frac{\partial^2 V(\mathbf{q})}{\partial \mathbf{q}^2}\mathbf{M_{qp}} & -\frac{\partial^2 V(\mathbf{q})}{\partial \mathbf{q}^2}\mathbf{M_{qq}} \\ +\frac{\partial^2 T(\mathbf{p})}{\partial \mathbf{p}^2}\mathbf{M_{pp}} & +\frac{\partial^2 T(\mathbf{p})}{\partial \mathbf{p}^2}\mathbf{M_{pq}} \end{pmatrix}, \tag{A.5}$$

we write Equation (A.1) as

$$\begin{aligned} A^{-1}(t)\dot{A}(t) =& \frac{1}{2}\mathrm{tr}\left(\frac{\dot{\mathbf{M}}_{\mathbf{qq}} + i\dot{\mathbf{M}}_{\mathbf{pq}} + \dot{\mathbf{M}}_{\mathbf{pp}} - i\dot{\mathbf{M}}_{\mathbf{qp}}}{\mathbf{M_{qq}} + i\mathbf{M_{pq}} + \mathbf{M_{pp}} - i\mathbf{M_{qp}}}\right) \\ =& \frac{1}{2}\mathrm{tr}(\Lambda(t)^{-1}\dot{\Lambda}(t)). \end{aligned} \tag{A.6}$$

Our aim is to show that equation (A.6) is the same equation of motion as that of the Herman-Kluk prefactor, $R(t)$ . $R(t)$ evolves according to[34]

$$\begin{aligned} R(t) =& \det\left(\frac{1}{2}(\mathbf{M_{pp}} + \mathbf{M_{qq}} - i\mathbf{M_{qp}} + i\mathbf{M_{pq}})\right)^{\frac{1}{2}} \\ =& \det\left(\frac{\Lambda(t)}{2}\right)^{\frac{1}{2}}. \end{aligned} \tag{A.7}$$

To show that this is equivalent to equation A.6, we begin by taking the first derivative of $R(t)$,

$$\dot{R}(t) = \frac{1}{2}R(t)^{-1}\frac{\mathrm{d}}{\mathrm{d}t}\det\left(\frac{\Lambda(t)}{2}\right). \tag{A.8}$$

The derivative of the determinant can be found by expressing it in the form

$$\begin{aligned} \frac{\mathrm{d}}{\mathrm{d}t}\det\left(\frac{\Lambda(t)}{2}\right) &= \lim_{\delta t\to 0}\frac{\det\left(\frac{\Lambda(t+\delta t)}{2}\right) - \det\left(\frac{\Lambda(t)}{2}\right)}{\delta t} \\ &= \lim_{\delta t\to 0}\frac{\det\left(\frac{\Lambda(t)}{2}\right)\left(\det\left(\mathrm{I} + \frac{\delta t}{2}\Lambda(t)^{-1}\dot{\Lambda}(t) + \ldots\right) - 1\right)}{\delta t} \end{aligned} \tag{A.9}$$

and expanding to first order in $\delta t$ we get that,

$$\begin{aligned}
\det(\mathrm{I}+\frac{\delta t}{2}\Lambda(t)^{-1}\dot{\Lambda}(t)+\ldots) &= \prod_{k=1}^{N}(1+\frac{\delta t}{2}(\Lambda(t)^{-1}\dot{\Lambda}(t))_k)+\mathcal{O}(\delta t^2) \\
&= 1+\delta t\sum_{k=1}^{N}(\Lambda(t)^{-1}\dot{\Lambda}(t))_k+\mathcal{O}(\delta t^2) \\
&= 1+\delta t\,\mathrm{tr}(\Lambda(t)^{-1}\dot{\Lambda}(t))+\mathcal{O}(\delta t^2), \qquad \text{(A.10)}
\end{aligned}$$

so that equation (A.9) becomes

$$\begin{aligned}
\frac{\mathrm{d}}{\mathrm{d}t}\det\Big(\frac{\Lambda(t)}{2}\Big) &= \lim_{\delta t\to 0}\frac{\det\big(\frac{\Lambda(t)}{2}\big)(1+\delta t\,\mathrm{tr}(\Lambda(t)^{-1}\dot{\Lambda}(t))+\mathcal{O}(\delta t^2)-1)}{\delta t} \\
&= \lim_{\delta t\to 0}\det\Big(\frac{\Lambda(t)}{2}\Big)(\mathrm{tr}(\Lambda(t)^{-1}\dot{\Lambda}(t))+\mathcal{O}(\delta t) \\
&= \det\Big(\frac{\Lambda(t)}{2}\Big)\mathrm{tr}(\Lambda^{-1}(t)\dot{\Lambda}(t)\big), \qquad \text{(A.11)}
\end{aligned}$$

which, from Equation (A.8), gives that

$$R^{-1}(t)\dot{R}(t)=\frac{1}{2}\mathrm{tr}\big(\Lambda(t)^{-1}\dot{\Lambda}(t)\big). \qquad \text{(A.12)}$$

Equation (A.12) is the same as (A.6), which proves that $A(t)$ and $R(t)$ indeed have the same equations of motion. They can be exactly related by noting that $R(0)=1$, so $R(t)=\frac{A(t)}{A(0)}$. Substituting this into the expression derived by Lu and Zhou[18], we arrive at our expression for $\left|\phi_t^k\right\rangle$ given in equation (2.27).

# Appendix B

We present the set of parameters for the 24 mode model which were used in the MCTDH and FGA-SH simulations that are presented in chapter 5 of this thesis. A full account of the parameters, which are derived from a combination of experimental and ab initio methods is given in the original paper by Raab et al.[21] The energy gap between the $S_1$ and $S_2$ states was taken to be its experimental value, $2\Delta = 0.8460$eV, as were the vibrational frequencies. These quantities were experimentally determined using picosecond fluorescence.[26].

All other parameters were determined using the Single-Excitation Configuration Interaction (CIS) method, except where the need for accuracy demanded the use of the higher level complete-active-space self-consistent field (CASSCF) method. We mark those parameters taken from CASSCF calculations with $^*$. Furthermore, one of the linear on-diagonal parameters, $\kappa^{(2)}_{\nu_1}$ was adjusted in order to better reproduce the $S_2$ spectrum, which is denoted $^\dagger$.

The data is divided up into three sections. The vibrational frequencies are presented given in Section B.1, linear and quadratic on-diagonal constants in Section B.2, and linear and quadratic off-diagonal constants in Section B.3. Only the non-zero elements are given for each set. All parameters are given in units of eV.

## B.1 Vibrational Frequencies

| Mode | Frequency (eV) | Mode | Frequency (eV) | Mode | Frequency (eV) |
|---|---|---|---|---|---|
| $\nu_{10a}$ | 0.1139 | $\nu_{6b}$ | 0.0873 | $\nu_{19a}$ | 0.1840 |
| $\nu_1$ | 0.1258 | $\nu_3$ | 0.1669 | $\nu_{13}$ | 0.3734 |
| $\nu_2$ | 0.3788 | $\nu_{8b}$ | 0.1891 | $\nu_{18b}$ | 0.1318 |
| $\nu_{6a}$ | 0.0739 | $\nu_{7b}$ | 0.3769 | $\nu_{14}$ | 0.1425 |
| $\nu_{8a}$ | 0.1961 | $\nu_{16a}$ | 0.0423 | $\nu_{19b}$ | 0.1756 |
| $\nu_{9a}$ | 0.1525 | $\nu_{17a}$ | 0.1190 | $\nu_{20b}$ | 0.3798 |
| $\nu_4$ | 0.0937 | $\nu_{12}$ | 0.1266 | $\nu_{16b}$ | 0.0521 |
| $\nu_5$ | 0.1219 | $\nu_{18a}$ | 0.1408 | $\nu_{11}$ | 0.0973 |

## B.2 On-diagonal terms

### B.2.1 Linear

| | $\nu_1$ | $\nu_2$ | $\nu_{6a}$ | $\nu_{8a}$ | $\nu_{9a}$ |
|---|---|---|---|---|---|
| $\kappa^{(1)}$(eV) | −0.0503 | 0.0247 | −0.0981 | −0.0445 | 0.1452 |
| $\kappa^{(2)}$(eV) | $-0.17100^{\dagger}$ | 0.0162 | 0.1355 | 0.0168 | 0.0375 |

### B.2.2 Quadratic

| $\gamma^{(1)}$(eV) | $\nu_1$ | $\nu_2$ | $\nu_{6a}$ | $\nu_{8a}$ | $\nu_{9a}$ |
|---|---|---|---|---|---|
| $\nu_1$ | −0.00810 | −0.00163 | 0.00108 | 0.00154 | 0.00474 |
| $\nu_2$ |  | −0.00118 | −0.00285 | −0.00143 | −0.00474 |
| $\nu_{6a}$ |  |  | 0.00002 | −0.00135 | −0.00204 |
| $\nu_{8a}$ |  |  |  | 0.00028 | 0.00872 |
| $\nu_{9a}$ |  |  |  |  | −0.00116 |

| $\gamma^{(2)}$(eV) | $\nu_1$ | $\nu_2$ | $\nu_{6a}$ | $\nu_{8a}$ | $\nu_{9a}$ |
|---|---|---|---|---|---|
| $\nu_1$ | 0.00488 | −0.00600 | −0.00298 | 0.00311 | 0.00155 |
| $\nu_2$ |  | 0.00039 | −0.00128 | −0.00713 | −0.00334 |
| $\nu_{6a}$ |  |  | −0.00917 | −0.00203 | −0.00189 |
| $\nu_{8a}$ |  |  |  | 0.01272 | 0.01194 |
| $\nu_{9a}$ |  |  |  |  | 0.00022 |

| $\gamma^{(1)}$(eV) | $\nu_{12}$ | $\nu_{18a}$ | $\nu_{19a}$ | $\nu_{13}$ |
|---|---|---|---|---|
| $\nu_{12}$ | −0.04819 | 0.00525 | −0.00485 | −0.00326 |
| $\nu_{18a}$ |  | −0.00792 | 0.00852 | 0.00888 |
| $\nu_{19a}$ |  |  | −0.02429 | −0.00443 |
| $\nu_{13}$ |  |  |  | −0.00492 |

| $\gamma^{(2)}$(eV) | $\nu_{12}$ | $\nu_{18a}$ | $\nu_{19a}$ | $\nu_{13}$ |
|---|---|---|---|---|
| $\nu_{12}$ | −0.00840 | 0.00536 | −0.00097 | 0.00034 |
| $\nu_{18a}$ |  | 0.00429 | 0.00209 | −0.00049 |
| $\nu_{19a}$ |  |  | −0.00734 | 0.00346 |
| $\nu_{13}$ |  |  |  | 0.00062 |

| $\gamma^{(1)}$(eV) | $\nu_{6b}$ | $\nu_3$ | $\nu_{8b}$ | $\nu_{7b}$ |
|---|---|---|---|---|
| $\nu_{6b}$ | −0.00741 | 0.01321 | −0.00717 | 0.00515 |
| $\nu_3$ | | 0.05183 | −0.03942 | 0.00170 |
| $\nu_{8b}$ | | | −0.05733 | −0.00204 |
| $\nu_{7b}$ | | | | −0.0033 |

| $\gamma^{(2)}$(eV) | $\nu_{6b}$ | $\nu_3$ | $\nu_{8b}$ | $\nu_{7b}$ |
|---|---|---|---|---|
| $\nu_{6b}$ | −0.00385 | −0.00661 | 0.00429 | −0.00246 |
| $\nu_3$ | | 0.04842 | −0.03034 | −0.00185 |
| $\nu_{8b}$ | | | −0.06332 | −0.00388 |
| $\nu_{7b}$ | | | | −0.00040 |

| $\gamma^{(1)}$(eV) | $\nu_{18b}$ | $\nu_{14}$ | $\nu_{19b}$ | $\nu_{20b}$ |
|---|---|---|---|---|
| $\nu_{18b}$ | −0.00277* | 0.00016* | −0.00250 | 0.00357 |
| $\nu_{14}$ | | 0.03924* | −0.00197 | −0.00355 |
| $\nu_{19b}$ | | | 0.00992 | 0.00623 |
| $\nu_{20b}$ | | | | −0.00110 |

| $\gamma^{(2)}$(eV) | $\nu_{18b}$ | $\nu_{14}$ | $\nu_{19b}$ | $\nu_{20b}$ |
|---|---|---|---|---|
| $\nu_{18b}$ | −0.01179* | −0.00844* | 0.07843 | −0.01249 |
| $\nu_{14}$ | | 0.0400* | −0.05000* | 0.00265 |
| $\nu_{19b}$ | | | 0.01246 | −0.00422 |
| $\nu_{20b}$ | | | | 0.00069 |

| $\gamma^{(1)}$(eV) | $\nu_{16a}$ | $\nu_{17a}$ |
|---|---|---|
| $\nu_{16a}$ | 0.01145* | 0.00100 |
| $\nu_{17a}$ |  | −0.02040 |
| $\gamma^{(2)}$(eV) | $\nu_{16a}$ | $\nu_{17a}$ |
| $\nu_{16a}$ | −0.01459* | −0.00091 |
| $\nu_{17a}$ |  | −0.00618 |

| $\gamma^{(1)}$(eV) | $\nu_{16b}$ | $\nu_{11}$ |
|---|---|---|
| $\nu_{16b}$ | −0.02176 | −0.00624 |
| $\nu_{11}$ |  | 0.00315 |
| $\gamma^{(2)}$(eV) | $\nu_{16b}$ | $\nu_{11}$ |
| $\nu_{16b}$ | −0.02214 | −.00261 |
| $\nu_{11}$ |  | −0.00496 |

| $\gamma^{(1)}$(eV) | $\nu_{4}$ | $\nu_{5}$ |
|---|---|---|
| $\nu_{4}$ | −0.02252* | −0.00049 |
| $\nu_{5}$ |  | −0.01825 |
| $\gamma^{(2)}$(eV) | $\nu_{4}$ | $\nu_{5}$ |
| $\nu_{4}$ | −0.03445* | 0.00911 |
| $\nu_{5}$ |  | −0.00265 |

| $\gamma^{(1,2)}$(eV) | $\nu_{10a}$ |
|---|---|
| $\nu_{10a}$ | −0.01159 |

## B.3 Off-diagonal terms

### B.3.1 Linear

| | $\nu_{10a}$ |
|---|---|
| $\lambda^{(1,2)}$(eV) | 0.2080 |

### B.3.2 Quadratic

| $c_{i,j}$(eV) | $\nu_1$ | $\nu_2$ | $\nu_{6a}$ | $\nu_{8a}$ | $\nu_{9a}$ |
|---|---|---|---|---|---|
| $\nu_{10a}$ | −0.00551 | −0.00512 | −0.01000* | 0.00799 | 0.00127 |

| $c_{i,j}$(eV) | $\nu_{6b}$ | $\nu_3$ | $\nu_{8b}$ | $\nu_{7b}$ |
|---|---|---|---|---|
| $\nu_4$ | −0.01372 | −0.00466 | 0.00329 | −0.00031 |
| $\nu_5$ | 0.00598 | −0.00914 | 0.00961 | 0.00500 |

| $c_{i,j}$(eV) | $\nu_{12}$ | $\nu_{18a}$ | $\nu_{19a}$ | $\nu_{13}$ |
|---|---|---|---|---|
| $\nu_{16a}$ | −0.01056 | 0.00559 | 0.00401 | −0.00226 |
| $\nu_{17a}$ | −0.01200 | −0.00213 | 0.00328 | −0.00396 |

| $c_{i,j}$(eV) | $\nu_{18b}$ | $\nu_{14}$ | $\nu_{19b}$ | $\nu_{20b}$ |
|---|---|---|---|---|
| $\nu_{16b}$ | 0.00118 | −0.00009 | −0.00285 | −0.00095 |
| $\nu_{11}$ | 0.01281 | −0.01780 | 0.00134 | −0.00481 |